UCLouvain

École polytechnique de Louvain

Microstructural analysis of Paramagnetic Rim Lesions in Multiple Sclerosis using diffusion-weighted Magnetic Resonance Imaging

Author: **Jules Detobel**
Supervisors: **Pietro Maggi, Benoit Macq, Laurence Dricot**
Readers: **Colin Vanden Bulcke, Cyril De Bodt**
Academic year 2021–2022
Master [120] in Biomedical Engineering

Acknowledgements

I wish to express my gratitude to my supervisors, Pr. Pietro Maggi, Pr. Benoit Macq and Pr. Laurence Dricot, for allowing me to work on this interesting subject, Multiple Sclerosis Research.

I am deeply indebted to Colin Vanden Bulcke for all the advice and hours he gave me to enable me to complete this master thesis.

I would also like to thank Maxence Wynen, Quentin Dessain, Manon Dausort, Océane Perdaens and Lukas Swieboda for the help they gave me.

Finally, I would like to thank my family and friends for the support they have given me throughout my academic career.

Abstract

Multiple Sclerosis (MS) is the most prevalent inflammatory disease of the central nervous system and Magnetic Resonance Imaging (MRI) is the go-to technique to assess this pathology in vivo. However, studying this type of pathology requires the acquisition of multiple MRI sequences, resulting in a large set of complex data in a non-standardized format. Moreover, the MRI techniques currently used in the clinic only partially correlate to MS disease severity and have thus limited prognostic relevance. In this context, identifying novel predictive MRI biomarkers, with a stronger correlation with clinical outcomes is needed. To address these issues, the BIDS Managing and Analysis Tool (BMAT) has been developed. It provides researchers with a user-friendly interface to create and manage datasets using the Brain Imaging Data Structure (BIDS), a format proposing a universal standard for naming and organizing neuroimaging data. In addition, this application allows the integration of different processing pipelines allowing to study advanced and pathologically more specific biomarkers of the disease. In the framework of this master thesis, a brain lesions segmentation pipeline giving information about the volumetry and location of brain lesions was integrated into BMAT. BMAT also allows for the analysis of paramagnetic rim lesions (PRL), a novel MRI biomarker which strongly correlate with patient's clinical disability. This thesis focused on characterizing PRL's microstructural changes using advanced diffusion-weighted MRI (DW-MRI). In 22 MS patients, we compared PRLs with control lesions using different microstructural models (DTI, NODDI, DIAMOND, MF) and found significant microstructural differences between these two types of lesions. In agreement with previous studies, this master thesis provides additional evidence that PRLs are associated with a more severe tissue damage in terms of axonal injury and inflammatory demyelination.

Keywords: Multiple Sclerosis, MS biomarkers, BIDS, MRI, Diffusion imaging

Contents

List of Figures

List of Tables

Abbreviations

AD Axial Diffusivity.

ADC Apparent Diffusion Coefficient.

ANTs Advanced Normalization Tools.

BIDS Brain Imaging Data Structure.

BMAT BIDS Managing Analysis Tool.

CIS Clinically Isolated syndrome.

CL Cortical Lesions.

CNS Central Nervous System.

CSF Cerebrospinal Fluid.

DIAMOND DIstribution of 3D Anisotropic MicrOstructural eNvironments in Diffusion-compartment imaging.

DTI Diffusion Tensor Imaging.

DW-MRI Diffusion-Weighted MRI.

FA Fractional Anisotropy.

FID Free Induction Decay.

GM Gray Matter.

GUI Graphical user interface.

JSON JavaScript Object Notation.

MD Mean Diffusivity.

MF Microstructure Fingerprinting.

MRI Magnetic Resonance Imaging.

MS Multiple Sclerosis.

NAGM Normal Appearing Gray matter.

NIfTI Neuroimaging Informatics Technology Initiative.

NODDI Neurite Orientation Dispersion and Density Imaging.

PGSE Pulsed Gradient Spin Echo.

PPMS Primary Progressive MS.

PRL Paramagnetic Rim Lesions.

RD Radial Diffusivity.

RF-Pulse Radiofrequency pulse.

RIS Radiologically isolated syndrome.

RRMS Relapsing-Remitting MS.

SPMS Secondary Progressive MS.

TE Echo Time.

TR Repetition Time.

WM White Matter.

Introduction

More than 2 million people worldwide are affected with Multiple Sclerosis (MS), the most prevalent chronic inflammatory disease of the Central Nervous System (CNS)[1]. Magnetic Resonance Imaging (MRI) is the go-to technique to assess MS pathologies in vivo, such as MS. Indeed, it allows to observe in vivo the pathological processes occurring in the brain of MS patients. However, the MRI techniques currently used in the clinic only partially correlate to MS disease severity and thus limited prognostic relevance. In this context, identifying novel predictive MRI biomarkers, with a stronger correlation with clinical outcomes is needed[2].

However, one of the main limiting factors for the advances in MS research is the fact that the study of neurological disorders often requires the acquisition of multiple MRI sequences, which results in a large set of complex data in a non-standardized format. This makes data sharing and reuse challenging, if not impossible and makes it more complex than necessary to implement automatic pipelines. A well-structured organization of neuroimaging data is then highly required. That's where the Brain Imaging Data Structure (BIDS) format comes in, by proposing a universal standard for naming and organizing neuroimaging data. The problem is that the dissemination and applicability of the BIDS format are limited due to the high number of restrictive rules needed to manage the whole variety of different neuroimaging data[3, 4].

To address this limitation, a software able to automatically implement the BIDS format has been developed by Colin Vanden Bulcke, a PhD student from the group in which I have been integrated to realize this master thesis. This software, called the BIDS Managing Analysis Tool (BMAT), provides researchers with a user-friendly interface to create and manage BIDS datasets automatically. Moreover, different analysis and processing pipelines can be integrated with it to perform tasks on the dataset in a fully automatic way[5].

In the context of my master thesis, the first objective was to add an existing brain lesions segmentation pipeline to BMAT. This segmentation pipeline gives as output a White Matter (WM) lesion mask as well as information about the brain and lesions

volumetry and location. Lesion segmentation being one of the fundamental tasks in MS MRI studies, the integration of such a pipeline to this application would allow searchers to use the information it outputs to study MRI biomarkers like Paramagnetic Rim Lesions (PRL).

PRLs are a specific type of brain WM lesions which are associated to a more severe tissue damage and to a more aggresive disease[6, 7]. Additionally, they seem to be useful for the diagnosis of MS since they appear to be relatively specific to the disease[8]. From a pathological point of view, PRLs are destructive lesions which tend to not remyelinate, to expand in size over time and are associated with a more severe axonal damage[2].

Due to their diagnostic and prognostic potential, it is of great interest to study PRLs. In the framework of this master thesis, the second objective was to study this biomarker with diffusion-weighted MRI (DW-MRI). DW-MRI is an advanced functional MRI method that enables the non-invasive generation of contrast by using the diffusion process of water molecules. It is based on the fact that water molecules' movements are constrained by the environment, including fibres, macromolecules and membranes. This technique can therefore be used to indirectly detect microstructural changes in tissues, making it a revolutionary tool for the diagnosis of pathological tissues[9].

The work on DW-MRI performed in the context of this thesis is intended to be an exploratory analysis, and will be followed by a larger-scale study to be carried out by the end of 2022. In this observational study, the goal is to use four distinct diffusion models and their metrics to characterize PRLs vs control brain WM lesions. These metrics can be translated in terms of WM integrity, axonal density and other tissue-integrity parameters, allowing to analyse and summarise the microstructural changes in PRLs vs. other lesions, and potentially giving new insights on the pathological characteristics of this novel biomarker.

This paper will be structured in the following way. The first part aims at giving all the theoretical background that is needed to understand the principles and methods used throughout this master thesis. This part is constituted by chapters about MS and MRI. The second part concerns the microstructural analysis with a first chapter describing the methods and materials used in this work. This chapter includes the description of the integration of the brain lesions segmentation pipeline to BMAT as well as the description of the microstructural analysis of PRLs using DW-MRI. The next chapter includes all the results of the microstructural analysis. The following chapter discusses the integration of the pipeline with BMAT as well as the results of the microstructural study and their interpretation and limitations. Finally, a global conclusion summarizing the important findings of this master thesis will be made.

Part I

State of The Art

Chapter 1

Medical context

1 Multiple sclerosis

More than 2 million people worldwide are affected by MS, the most prevalent chronic inflammatory disease of the CNS, which is currently incurable. It is a demyelinating disease of the CNS that typically affects individuals between the ages of 20 and 40[1]. As Fig.1.1 shows, the myelin sheath is a protective layer of lipids that is wrapped around the axon of neurons. This sheat allows the electrical impulses passing through the axons to travel quickly and efficiently and maintains the strength of this impulse all along the axon[10].

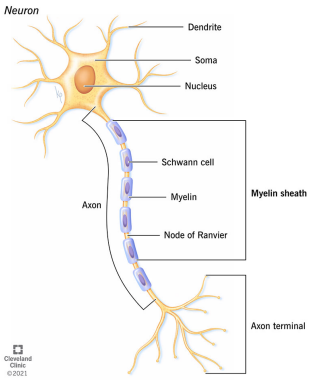

Figure 1.1: Structure of the myelin sheath within a nerve cell From [10]

In MS, demyelination happens when the immune system considers that myelin is a foreign substance. In this case, the body will produce inflammatory substances that will attack and eventually destroy the myelin. The result is a communication breakdown between neurons, which results in all sorts of sensory, motor and cognitive problems.

As it will be explained later, there are different subtypes of MS and early on in MS, the oligodendrocytes (cells responsible for the myelin sheath) will be able to heal and extend out new myelin to cover the neurons. This process is called remyelination. Unfortunately, over time as the oligodendrocytes die, the remyelination stops and the damage becomes irreversible with an axonal loss[11].

The exact cause of MS is unknown, but it is linked to both genetic and environmental factors. Genetics risk factors include being female and having genes associated to specific immunologic signatures. Environmental risk factors such as vitamin D deficiency and viral infection also play an important role[12]. A recent study found stronger evidence of the viral risk factor. Indeed, it seems that individuals infected with the Epstein-Barr virus, a human herpesvirus, are 32 times more likely to develop MS[13].

Specific symptoms largely depend on the location of the plaques and include vision loss, muscle weakness, tremor, lack of coordination, dysarthria, etc. Symptoms related to an attack can typically worsen over weeks and can linger for months without treatments.

MS is subdivided into clinical subtypes according to the pattern of symptoms over time. To explain the different subtypes, graphs with time (referring to the lifespan of the individual) on the x-axis and disability on the y-axis are used[14, 15]. (see Fig.1.2)

- **Clinically Isolated syndrome (CIS)**: It represents a first clinical episode that may evolve or not into MS. It concerns patients who have had an attack (an episode of symptoms) and are at risk of developing MS but for whom there is not yet sufficient evidence to diagnose as having MS.
- **Radiologically isolated syndrome (RIS)**: It concerns patients who show lesions typical to MS (WM lesions) on the MRI images but who have not yet developed symptoms.
- **Relapsing-Remitting MS (RRMS)**: It is the most common pattern of MS (85-90%). It is characterized by episodes of autoimmune attacks happening months or even years apart and causing an increase in the level of disability. After the attacks, it can be followed by a partial or a complete return to the initial state if there is remyelination. Unfortunately, most of the time the remyelination process is incomplete so there is often some residual disability that remains. That means that with each attack, more and more of the CNS gets irreversibly damaged. In the RRMS type, there is typically no increase in disability between the attacks.
- **Secondary Progressive MS (SPMS)**: Initially, it is similar to the RRMS but over time the immune attack becomes constant which causes a steady progression of disability. Most of the time, these are patients with RRMS evolving into SPMS.
- **Primary Progressive MS (PPMS)**: It is characterized by a constant attack on myelin which causes a steady progression of disability over a person's lifetime. It is typically noticeable on the scale of years.

The so-called "MS spectrum" is a collection of many neurological conditions sharing similar biochemical, clinical, and imaging features. Histopathological evidences support the hypothesis that MS is a heterogeneous disease. In particular, MS patients exhibit variation in both the disease's course and its response to treatment[16].

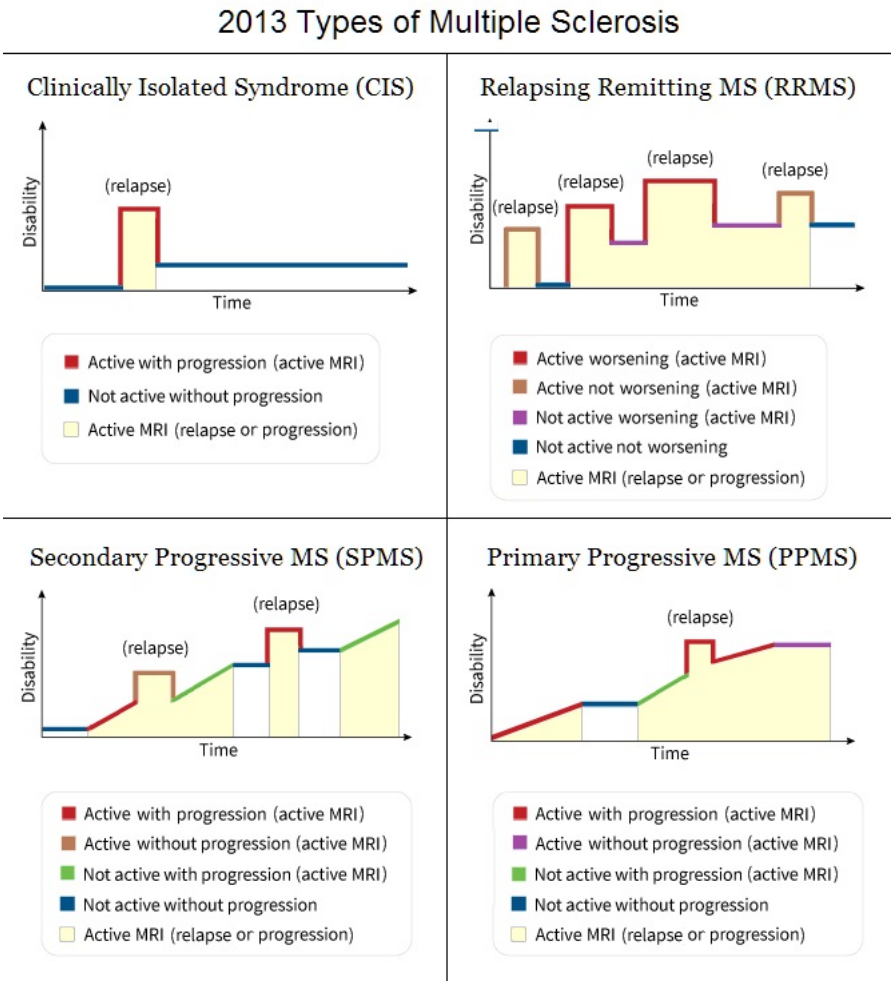

Figure 1.2: Illustration of the evolution of the disability in function of time for the different MS types. From [14]

2 Advanced prognostic MRI biomarkers in MS

Classic MRI metrics currently used in the clinic only partially correlate to MS disease severity and thus have limited prognostic relevance. These metrics include, among others[17]:

- The number of WM lesions: a high number can be associated with disability progression, aggressive course and conversion from CIS to RRMS.
- The total volume of lesions: it is associated with disability and cognitive/motor outcomes at long term follow-up.
- The rate of lesional volume growth: Some studies show that this rate is 3 times higher in SPMS compared to RRMS.
- The lesion location is predictive of disability.

Recent advances in MR technology have allowed the discovery of new specific prognostic MS biomarkers. Among them, 2 are of great interest : Paramagnetic Rim Lesions (PRL) and Cortical Lesions (CL). According to some studies, patients with PRLs experience an earlier progression of disability, whereas CL is linked to cognitive impairments. However, these biomarkers are only identified with the help of specific MRI sequences and it takes an experienced rater for their manual assessment, which can be very time-consuming. This is why many automation or semi-automation methods based on machine learning have been developed in recent years to try to facilitate and accelerate the evaluation of these new biomarkers[2]. These two biomarkers will be described in the rest of this section.

2.1 Paramagnetic Rim Lesions

Studies have shown that axonal loss and smouldering demyelination are present surrounding an inactive hypocellular core in about 30% of chronic demyelinated lesions, which are pathologically characterized by perilesional buildup of iron-laden microglia and macrophages (see illustration of this lesion type on Fig.1.3). Theses lesions are known as "chronic active/smouldering lesions" and can be detected in vivo using MRI as paramagnetic rim lesions (PRL). Indeed, given their peripheral paramagnetic iron rim, PRL can be detected using susceptibility-based MRI sequence is used (T2*-weighted magnitude, phase images and quantitative susceptibility mapping-QSM)[2, 18, 19].

PRLs are interesting for their prognostic indications. Indeed, recent studies have shown that a higher PRL burden is related to a more aggressive disease course and disability accumulation at a younger age and/or shorter disease duration[6]. This link between PRLs and disability is due to the nature of these lesions: these are destructive

lesions that do not remyelinate and expand in size over time, causing the demyelination of the surrounding tissues and then axonal damages. Since the paramagnetic rim has been shown to tend to fade over a median of 7 years, PRLs can serve as a proxy for the outcomes of clinical studies aiming at reducing inflammation around the edges of these chronic active lesions using specific disease modifying treatments[8, 7].

Moreover, PRLs also seem to be useful for the diagnosis of MS since they appear to be relatively specific to the disease. Indeed, there are only a few cases where these lesions have been detected in other diseases than MS (52% of patients with MS compared to 7% of non-MS in a study regrouping 438 patients)[8]. PRL have the potential to develop into a therapeutically useful biomarker to enhance MS diagnosis and track treatment effectiveness over time.

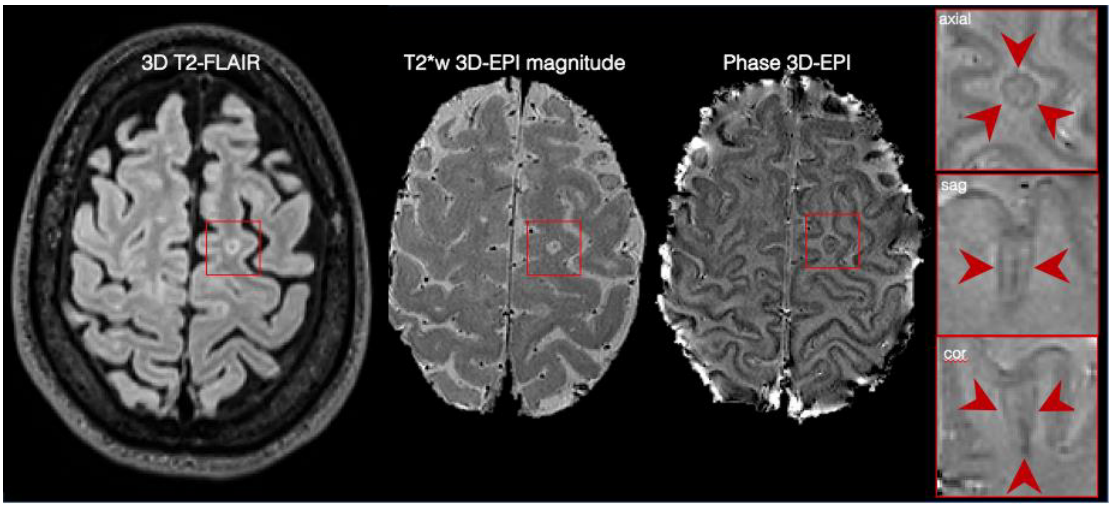

Figure 1.3: Illustation of PRL. From [2]

2.2 Cortical Lesions

Cortical lesions are focal lesions inside the cortex. They are classified into three main categories (See Fig.1.4)[2, 18]:

- Leukocortical lesions (Type I): Located at the interface between the cortex and the WM.
- Intracortical lesions (Type II): Purely located in the cortex without reaching the pial surface.
- Subpial lesions (Type III and IV): Located in the cortex and touching the subpial surface of the brain (type III) and sometimes extending to the WM (type IV).

Juxtacortical lesions can also be included in this section, they are WM lesions in direct contact with the cortex without intervening normal WM. Ageing and MS mimicking diseases (such as Neuromyelinitis optica and migraine) also cause lesions that are close to the cortex. However, in these conditions, lesions are frequently in the deep WM, with a rim of WM enclosing them and separating them from the cortex[2, 20].

CL are usually well depicted using T2-FLAIR in the clinical routine but to have better detection and localization of them, other specialized MRI sequences have been developed. These specialized sequences, which are more sensitive include Double Inversion Recovery (DIR) or T1-weighted Magnetization Prepared Rapid Gradient Echo (MPRAGE) or MP2RAGE. Due to their pathological features, it is quite challenging to detect CL. That is why guidelines based on lesion signal characteristics and size have been developed on DIR images. The criteria for the definition of a cortical lesion on DIR images are: (i) Hyperintensity compared to adjacent Normal Appearing Gray matter (NAGM) (ii) Size of at least 3 pixels along the main in-plane axis based on at least $1mm^2$ in-plane resolution. On PSIR and MPRAGE sequences, CL appears hypointense in comparison to the surrounding Gray Matter (GM) and they must involve the cortex[18, 20, 21].

The location of CL is considered typical of MS and there are several reasons that explain their potential to serve as a prognostic MRI biomaker:

1. They have been observed in the early stages of the disease, making them an indicator of conversion from CIS to MS[22].

2. They are linked to impairment, and in certain studies, their quantity was more strongly linked to cognitive disability than WM lesions[23].

3. Longitudinal studies have linked them with disease progression[24].

4. Subpial cortical demyelination is highly specific to MS making CL a powerful biomarker for the differential diagnosis of MS[25].

It is still challenging to visualize CL using standard clinical MRI sequences. Even for the most sensitive sequences, manual segmentation is quite time-consuming and prone to important inter-rater variability because CL are small and frequently subtle[2, 20].

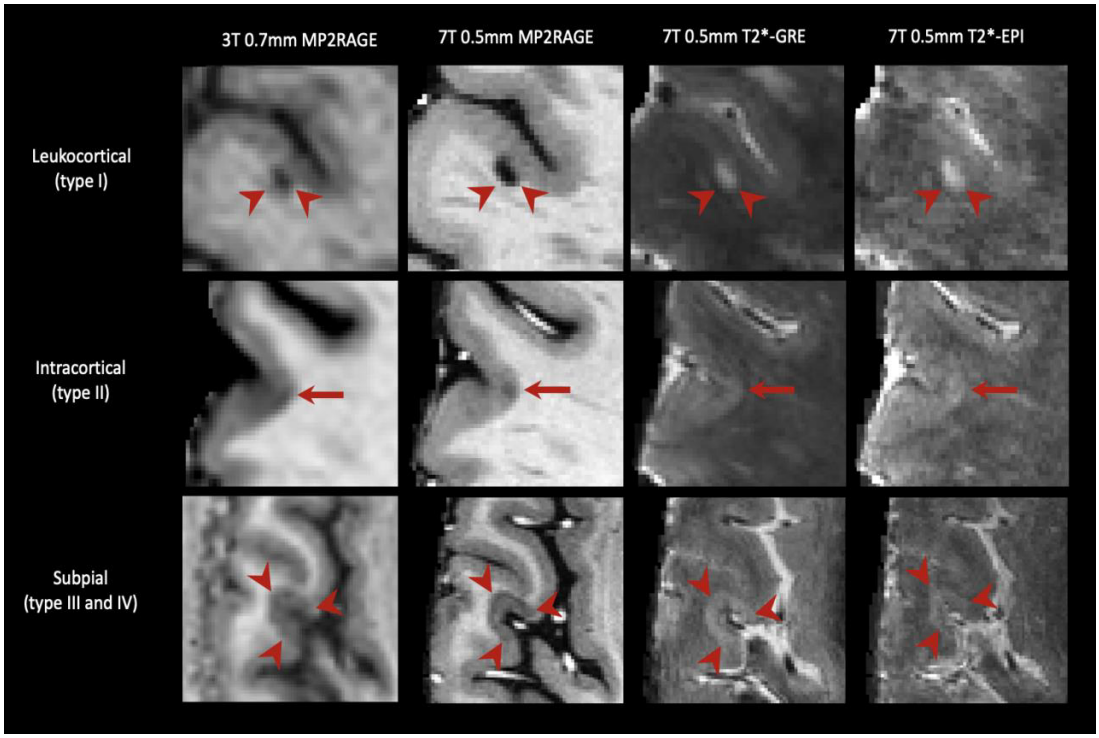

Figure 1.4: Illustration of the different CL types. From [2]

Chapter 2

Magnetic resonance imaging

MRI is an imaging technique based on electromagnetism that combines mathematical and computational tools to reconstruct structural and functional images of the brain. This imaging technique was invented in 1971 by Paul C. Lauterbur. This is a non-invasive and non-irradiating technique that is useful to study the structure of the brain but also some cognitive processes.[26, 27]

1 Magnetic resonance imaging

1.1 Magnetic properties

MRI is based on the magnetic properties of the hydrogen atoms, which are formed of a negatively charged particle, an electron and a positively charged one, a proton. The proton is a particle that has the particularity of spinning on itself. This movement is called a spin and is a form of intrinsic angular momentum. The technology is based on hydrogen because it represents $2/3$ of the human body nucleus and has a large intrinsic magnetic moment. Since the proton is a charged particle rotating around its axis, it will produce an electric current which will be responsible for the creation of a magnetic field characterized by a magnetic moment μ oriented along its axis of rotation. As a result, the spin can be described as a small bar magnet[28]. (see Fig.2.1)

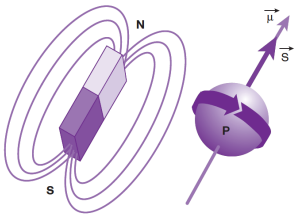

Figure 2.1: Representation of the spin and magnetic moment of a particle. [28]

In the absence of an external magnetic field, protons in tissues are randomly oriented resulting in a null macroscopic magnetization ($\sum \mu = \mathbf{0}$)(left part of Fig.2.2). However, if an external magnetic field $\mathbf{B_0}$ is applied, the magnetic moments of each nucleus will tend to align with this magnetic field either in a parallel (up, low energy state E_1) or anti-parallel way (down, high energy state E_2)(bottom part of Fig.2.2). Thus, resulting in a non-negligible macroscopic magnetization ($\sum \mu \neq \mathbf{0}$). According to quantum mechanics, there is only a discrete number of possible orientations for a spin in a magnetic field ($2I+1$). For the proton, $I = 1/2$, that's why there are only 2 possibilities for the hydrogen: parallel (spin up) and antiparallel (spin down)[28, 29].

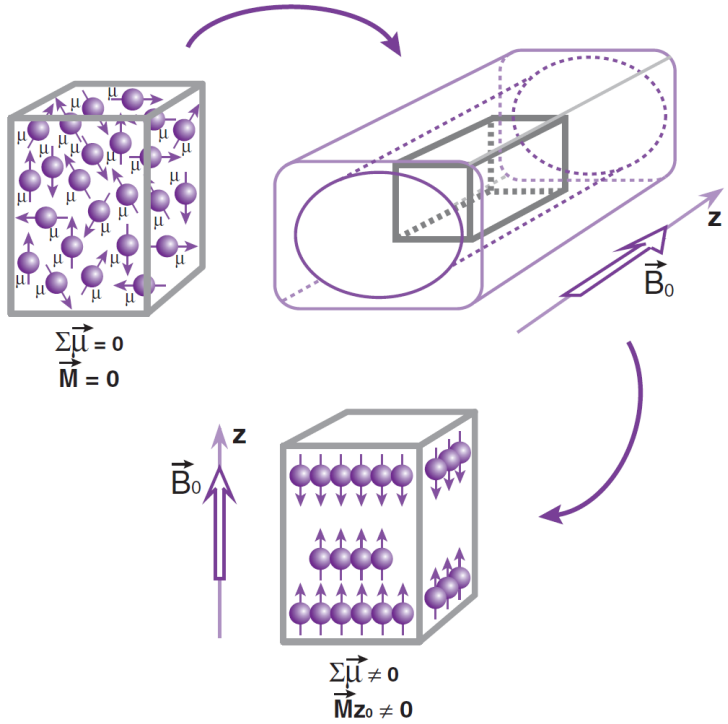

Figure 2.2: Influence of an external magnetic field on the magnetic moment orientation. [28]

In addition to that, the magnetic moment in the external magnetic field $\mathbf{B_0}$ will experiences a torque $\tau = \mu \times \mathbf{B_0}$. This torque is the reason why the protons are not perfectly oriented along the z-axis in a perfect parallel or antiparallel way. The result of this torque is a precession movement along the direction of $\mathbf{B_0}$ characterized by the Larmor frequency given by :

$$f_0 = \gamma B_0 \tag{2.1}$$

where γ is the gyromagnetic ratio (in Hz/T) which is characteristic for each nucleus ($42.58MHz/T$ for ^1H). This precession movement can be seen in Fig.2.3.

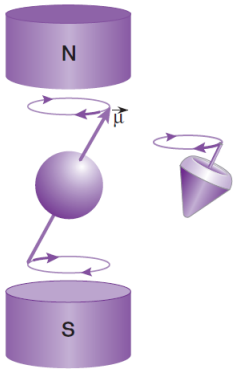

Figure 2.3: Precession movement of a spin submitted to an external magnetic field $\mathbf{B_0}$ [28]

Now there is a macroscopic magnetization that appears under the effect of an external magnetic field. It is possible to decompose this magnetization into a transverse and a longitudinal magnetization:

$$\mathbf{M} = \frac{1}{V}\sum_i \mu_\mathbf{i} = M_z \mathbf{1}_z \tag{2.2}$$

At the moment, if the external field $\mathbf{B_0}$ is considered constant and no other magnetic field is involved, the transverse magnetization M_{xy} is null. It is due to the spins having a random phase for their precession movement resulting in magnetic moments cancelling each other. However, it is not the case for longitudinal magnetization ($M_z \neq 0$). As mentioned earlier, there are two possible orientations for the hydrogen, each one corresponding to a different energy level. This difference in energy level is given by :

$$\Delta E = E_\downarrow - E_\uparrow = hf_0$$

with $h = 6.62607004 \times 10^{-34} m^2 kg/s$ the Planck's constant. There are more spins oriented up than down. It is because the spins up (parallel) are at a lower energy level and

are thus advantaged over the spins down (anti-parallel). The ratio between the number of spins up over the number of spins down is given by :

$$\frac{N_{\uparrow}}{N_{\downarrow}} = exp(\frac{\Delta E}{kT}) \tag{2.3}$$

This expression gives rise to the fact that the resulting macroscopic longitudinal magnetization is non-zero :

$$M_z = M_0 = \frac{\gamma h^2 \rho B_0 I(I+1)}{3kT} \tag{2.4}$$

with ρ the spin density, k the Boltzmann's constant, T the temperature [K].[30]

1.2 Magnetic resonance

At equilibrium, the macroscopic magnetization vector ($\mathbf{M}$) is aligned with the magnetic field ($\mathbf{B_0}$). Which means that only the longitudinal component of the magnetization vector is non zero ($M_z = M_0 \neq 0$ and $M_x = M_y = 0$). As equation (2.4) states, M_z increases with the protons density (ρ) per volume unit and with the intensity of B_0. The problem is that it is impossible to measure this macroscopic magnetization vector since it is really small in comparison to B_0. The goal is then to obtain a measurable signal. To do so, a time-varying Radiofrequency pulse (RF-Pulse) that oscillates at the Larmor frequency is used to move away the magnetization of the protons from the external magnetic field. The Larmor frequency refers to the rate of precession of the magnetic moment of the proton around the external magnetic field.[31]

$$\mathbf{B_1}(t) = 2B_1(t)cos(2\pi f_{RF} t + \phi)\mathbf{1_{xy}} \tag{2.5}$$

where $f_{RF} = f_0$ represents the frequency of the RF-pulse.

Since it oscillates at the Larmor frequency, this RF-pulse carries energy equal to ΔE that will allow a resonance phenomenon to appear. The RF-pulse causes the longitudinal magnetization to switch its orientation by inducing a change in the energy state of the spins. The result of this transition from one energy state to another is a transverse magnetization since the spins are in phase (due to the resonance phenomenon) during the excitation.

It is possible to observe the effect of the RF-pulse visually in the fixed and rotating frames in Fig 2.4. From a macroscopic point of view, the magnetization vector ($\mathbf{M}$) has a double precession movement (around $\mathbf{B_0}$ and $\mathbf{B_1}$). If we consider a frame rotating at the Larmor frequency (f_0), the movement of $\mathbf{M}$ can be seen as a simple shift with an angle called "flip angle" between the z-direction and $\mathbf{M}$.

$$\alpha = \gamma \int_{T_{RF}} B_1(t)dt \overset{B_1(t)cst}{=} \gamma B_1 T_{RF} \tag{2.6}$$

with T_{RF} the RF-pulse duration. Equation (2.6) shows that the flip angle depends on B_1 and T_{RF}. These are the two parameters that are tuned to obtain the two most important RF-pulses, the 90° and 180° pulses. The 90° pulse will cause the protons on the low energy level to go to the high energy level, causing the longitudinal magnetization to go to zero and the transversal one to be maximum (see Fig.2.5.B). The 180° pulse will cause the excess protons to shift from the high energy level to the low energy level, leading to the inversion of the longitudinal magnetization (see Fig.2.5.C).

Finally, the macroscopic magnetization is then given by:

$$\mathbf{M} = \frac{1}{V}\sum_i \mu_\mathbf{i} = M_z\mathbf{1}_z + M_{xy}\mathbf{1}_{xy} \tag{2.7}$$

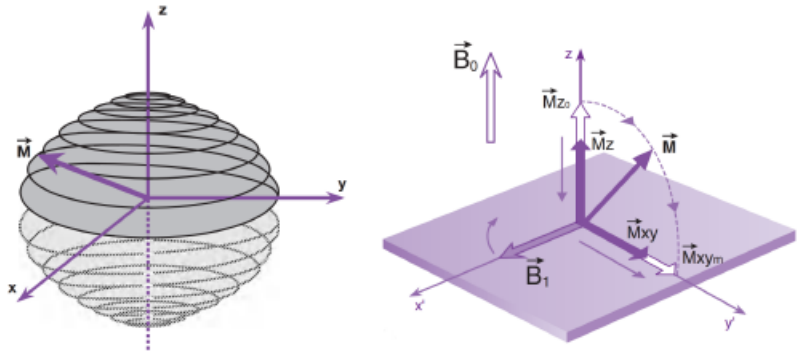

Figure 2.4: Double precession movement in the 2 frames. On the left is the fixed frame, on the right is the rotating frame [28]

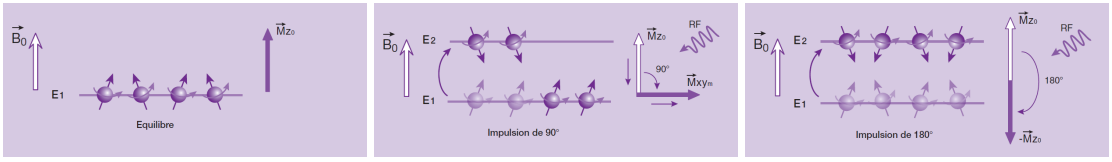

A B C

Figure 2.5: Representation of the macroscopic magnetization: A. In Resting State; B. After a 90° RF-pulse; C. After a 180° RF-pulse[28]

After the excitation, the spin system will go back to its equilibrium state (equation (2.4)). It means that the transversal magnetization ($\mathbf{M_{xy}}$) will disappear and the longitudinal magnetization will recover its value at equilibrium ($\mathbf{M_0}$). It is important to make a distinction between those two phenomena. The disappearance of $\mathbf{M_{xy}}$ is called the T2-relaxation, spin-spin relaxation or transversal relaxation and the reappearance of $\mathbf{M_z}$ is called T1-relaxation or longitudinal relaxation.

1.3 T1-Relaxation

As shown in figure 2.5, the 90° RF pulse excitation results in the disappearance of the longitudinal component M_z of the tissue magnetisation vector by equalisation of the spins on both energy levels. (transfer half of the excess spins from low energy level to high energy level). As soon as the RF pulse is stopped, there is a progressive return to an equilibrium state and then a progressive recovery of the longitudinal component of M. This relaxation is called T1-relaxation because it grows according to an exponential in T_1 given by:

$$M_z(t) = M_0 + (M_z(0) - M_0)e^{\frac{-t}{T_1}}, \tag{2.8}$$

where $M_z(0)$ is the longitudinal magnetization just after the RF-pulse, T_1 is a time constant and represents the time needed for the longitudinal magnetization to recover 63% of its amplitude[32]. The T1-relaxation can be seen on the left of Fig.2.6.

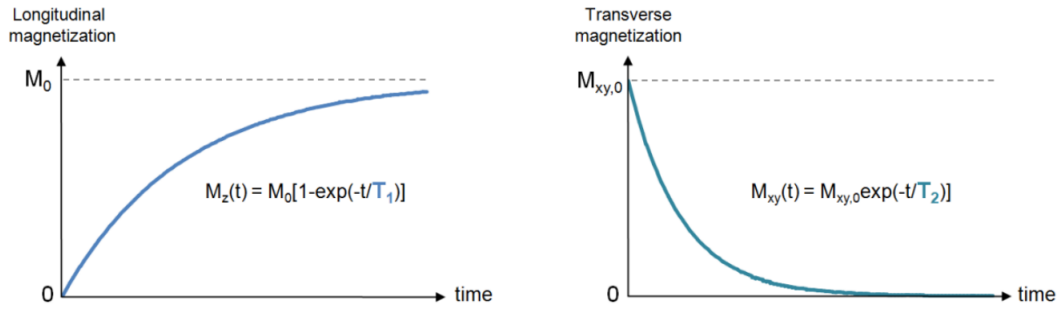

Figure 2.6: Relaxation rates of longitudinal magnetization (left) and transverse magnetization (right) [32]

This return to the equilibrium state will also emit energy to the lattice, which is why it is also called spin-lattice relaxation. The efficiency of this energy transfer will increase as the molecular collision frequency v_c gets closer and closer to f_0. If these frequencies are close then the relaxation is very efficient and thus T_1 is short. If the frequencies differ, the T_1 increases.(see Fig.2.7) Since v_c depends on each tissue, it is possible to observe a different response for each tissue, which will bring different contrasts to the images. These sequences based on T1 relaxation times are called "T1-weighted"[28, 32].

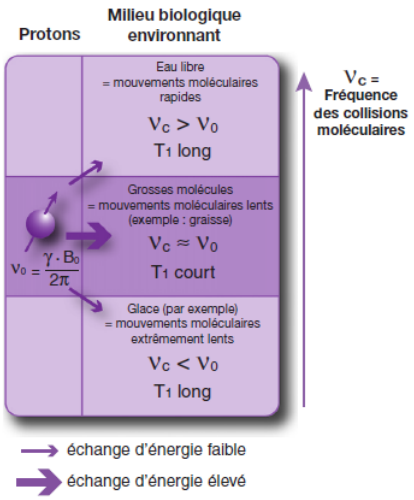

Figure 2.7: Efficiency of the energy exchange in function of the tissue composition [28]

1.4 T2-Relaxation

As already mentioned, the 90° RF-pulse results in the appearance of a transversal magnetization ($\mathbf{M_{xy}}$) due to a rephasing of the spins. Once the RF-pulse is stopped, there is a fast phase shift of the spins and the result is a fast disappearance of the transversal magnetization. This phenomenon is the consequence of an interaction between the protons, which is why it is also called spin-spin relaxation. It is important to mention that the protons evolve in different molecular environments where small magnetic fields will be superimposed on the main magnetic field $\mathbf{B_0}$. It will cause what is called field inhomogeneities from molecular origins. Due to these inhomogeneities, protons have small differences in their precession speed resulting in phase incoherence before and after the application of the RF-pulse. This relaxation is described by a decreasing exponential in T_2 (Fig2.6):

$$M_{xy}(t) = M_{xy}(0)e^{-\frac{t}{T_2}} \tag{2.9}$$

$M_{xy}(0)$ is the transversal magnetization just after the RF-pulse, T_2 is a time constant and represents the time needed for the transversal magnetization to lose 63% of its amplitude.

In addition to field inhomogeneities from the molecular origin, there are also inhomogeneities from "instrumental" origins. These inhomogeneities will cause a larger phase shift between the protons and the result is that the signal will decrease more rapidly according to an exponential in T_2^* (and not T_2) as can be observed on Fig2.8. This time constant is called the effective relaxation time and is given by the following expression:

$$\frac{1}{T_2^*} = \frac{1}{T_2} + \gamma \Delta B_0 \tag{2.10}$$

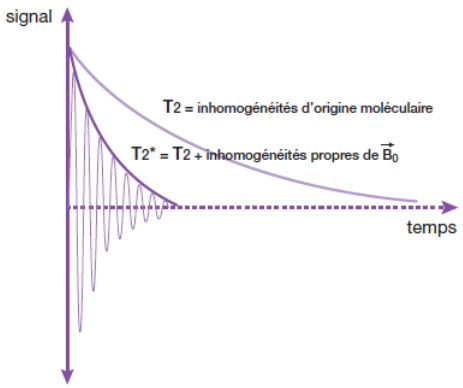

Figure 2.8: Comparison between T_2 and T_2^* [28]

As for the T_1-relaxation, T_2 depends on the tissue characteristics and the responses will then be different depending on the environment. Those T_2 differences will be useful for T_2-weighted sequences.

The global equation of motion of the nuclear magnetization, depending on T_1 and T_2 is known as the Bloch equations [33]:

$$\frac{dM_z}{dt} = -\frac{M_x}{T_2} + \Delta\omega M_y - \gamma B_{1y} M_z \tag{2.11}$$

$$\frac{dM_y}{dt} = -\Delta\omega M_x - \frac{M_y}{T_2} + \gamma B_{1x} M_z \tag{2.12}$$

$$\frac{dM_z}{dt} = \gamma B_{1y} M_x - \gamma B_{1x} M_y + \frac{M_0 - M_z}{T_1} \tag{2.13}$$

1.5 Spin echo sequence

What is measured in MRI is a Free Induction Decay (FID). This FID is related both to field inhomogeneities from molecular origins (spins-spins) and the inhomogeneities specific to the magnetic field $\mathbf{B_0}$ resulting in a signal decreasing exponentially with T_2^*[34]. However, the inhomogeneities specific to the magnetic field are undesirable and only the molecular interactions are of interest (represented in T_2). To this end, a method called "spin echo sequence" has been proposed to get rid of the inhomogeneities related to the "qualities" of the imager which weaken and reduce the signal duration as can be observed in Fig2.9.

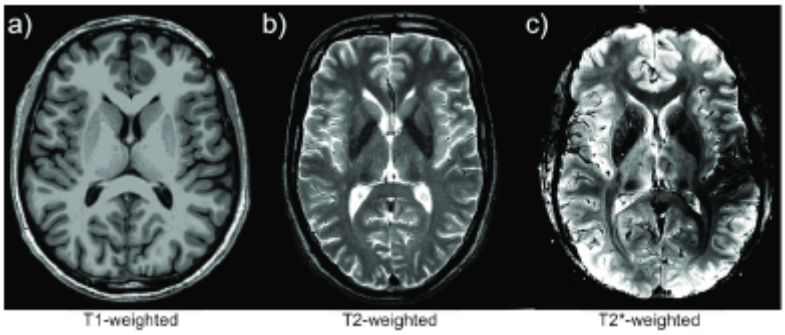

Figure 2.9: Difference between T_2 and T_2^* [35]

This spin-echo sequence is composed of a $90°$ followed by a $180°$ RF impulse as is represented in Fig.2.10. As the $180°$ impulse cancels the constant inhomogeneities related to $\mathbf{B_0}$, the Echo Time (TE) correspond to the time for the spins to be refocused with only the intrinsic spin-spin phase shift remaining and a signal reappears in the form of an echo. Another important parameter is the Repetition Time (TR) which corresponds to the time between two $90°$ RF impulses[28, 35].

It is important to note that one spin-echo cycle allows capturing only one line of the image matrix (image matrix corresponding to the k-space). The number of lines depends on the resolution of the imager. To obtain an image, spatial information has to be added to the signal by selecting a slice plane and defining the horizontal and vertical directions on this plane have to be defined. The RF signal is then processed according to this information to reconstruct the image.[36]

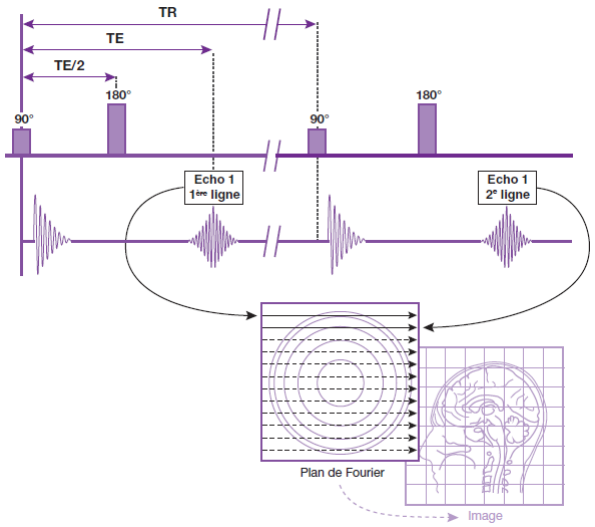

Figure 2.10: Spin Echo sequence [28]

The MRI contrast translates the differences in relaxation time and protons density. It is possible to play on the contrast by varying the TE and the TR since the images are weighted by a contrast factor c, depending on these two controlled parameters. If TE << TR, this contrast factor is given by :

$$c = M_0(1 - e^{-\frac{TR}{T_1}})e^{-\frac{TE}{T_2}} \tag{2.14}$$

Strong T_1 contrast can be obtained by using both a short TR and a short TE. In doing so, it is possible to highlight the difference in T_1 relaxation between the different tissues while keeping the T_2 contribution to a minimum as shown in the upper part of Fig.2.11.

On the contrary, it is possible to obtain an image with a strong T_2 contrast using a long TR and a long TE, as shown in the lower part of Fig.2.11.

It is also possible to obtain a proton density contrast by using a long TR and a short TE. In this manner, these are not the differences in relaxation time that are highlighted, the tissues with a higher proton density will display a stronger signal (see Fig.2.12).[36]

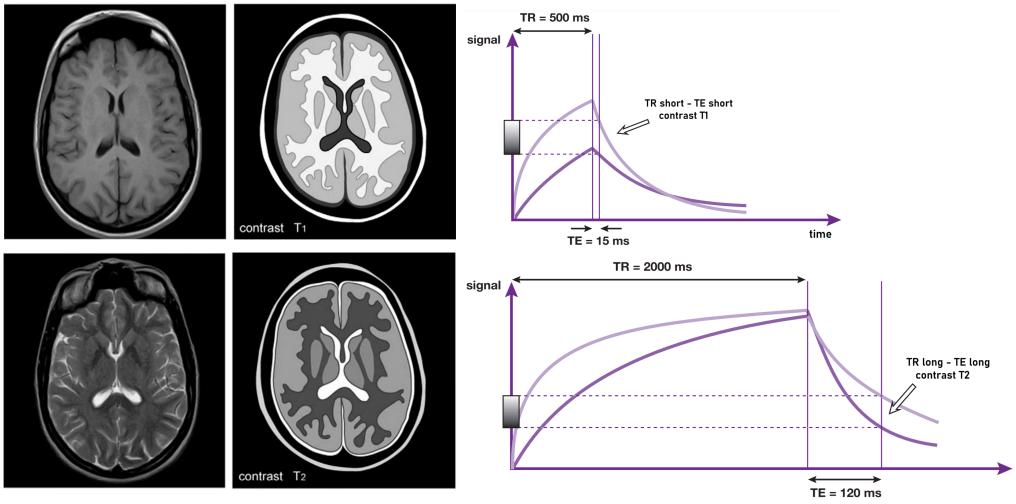

Figure 2.11: T_1 and T_2 contrasts, adapted from [28]

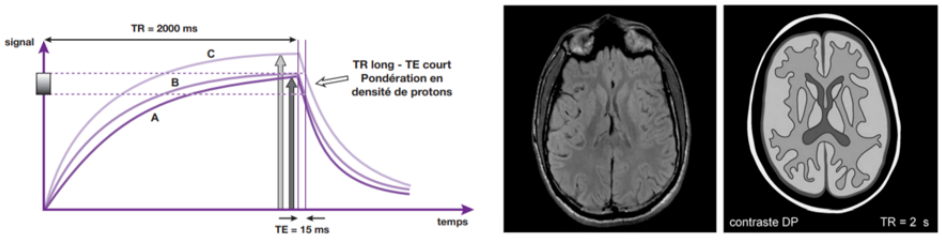

Figure 2.12: Proton density contrast, adapted from [28]

2 Diffusion-Weighted MRI

DW-MRI is an advanced functional MRI method that enables the non-invasive generation of contrast by using the diffusion process of molecules, mainly water. It is based on the fact that water molecules follow what is called a Brownian movement (random thermal movement) which is constrained by the environment, including fibres, macromolecules and membranes. DW-MRI can therefore be used to detect microstructural changes in tissues, making it a revolutionary tool for the diagnosis of different types of brain pathology[9].

2.1 Pulse Gradient Spin Echo

To have sequences sensitive to the diffusion, two supplementary gradients are added to a standard sequence like the spin echo to obtain what is called the Pulsed Gradient Spin Echo (PGSE) sequence. This sequence is the most commonly used in DW-MRI. PGSE sequences involve two gradients of constant magnitude applied back to back. As we can observe in Fig.2.13, the first gradient is applied just after the 90°RF-pulse to create a phase shift of the magnetization while the second one is applied after the 180°RF-pulse to allow the re-phasing of the magnetization.

The PGSE sequence can be characterized by 4 parameters:

- γ : The gyromagnetic ratio
- G : The magnitude of the diffusion gradients
- δ : The duration of the diffusion gradients
- Δ : The interval of time between the diffusion gradients.

These four parameters are part of the Stejskal-Tanner equation which gives the formula to obtain a single scalar characterizing the whole PGSE sequence.[9] This scalar is called the b-value and is given by:

$$b_{PGSE} = \gamma^2 G^2 \delta^2 (\Delta - \frac{\delta}{3}) [s/mm^2] \tag{2.15}$$

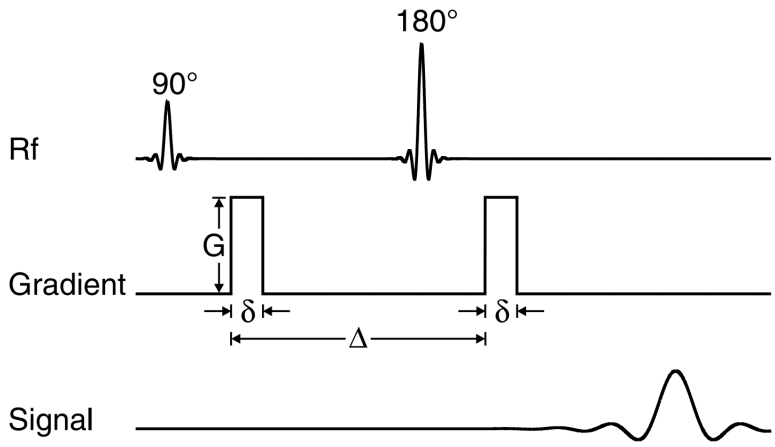

Figure 2.13: PGSE sequence. From [37]

Fig.2.14 represents the effect of the diffusion gradients from the PGSE sequence on the spins with and without water molecules diffusion. As already said, the second gradient allows to re-phase the spins but as some of them move due to diffusion, they will not be perfectly rephased and there will be a signal loss resulting in a darker signal in the image at locations where there is diffusion. The diffusion can be affected by several factors like the structure and composition of the tissue or the temperature. That's why the contrast in DW-MRI varies in the different structures. For example, since water molecules are free to move in every direction in the CSF, the diffusion in this region will be higher than in white matter (WM) where the diffusion is important in the axon's longitudinal axis but reduced in other directions. These differences in diffusion will result in an output signal that is darker in the CSF and lighter in WM. The imaging process has to be repeated multiple times with different gradient directions to deal with anisotropic diffusion. Indeed, most of the brain regions are characterized by a highly anisotropic diffusion and DW-MRI images are weighted by the diffusion of water molecules along the specific direction of the diffusion gradients[9].

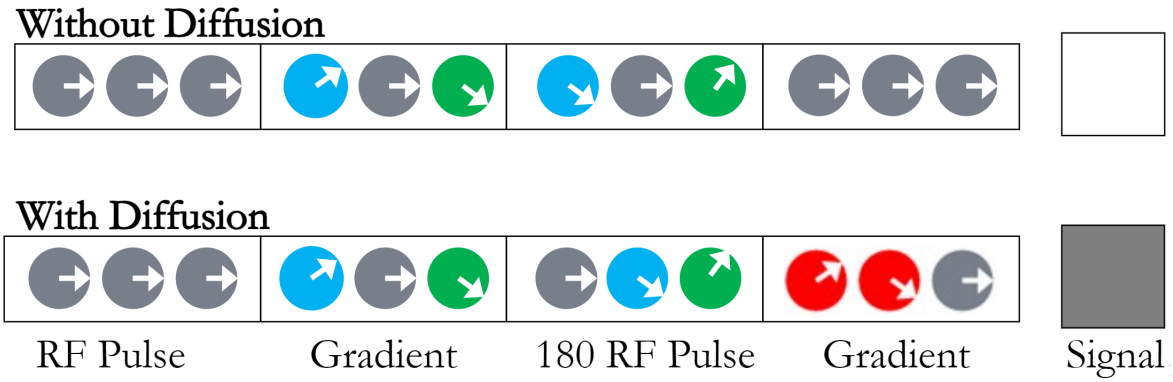

Figure 2.14: Effect of the PGSE sequence on the magnetization without and with diffusion. From [38]

Another interesting coefficient is the Apparent Diffusion Coefficient (ADC). This coefficient represents the rate of diffusion in biological tissues. To be able to compute this coefficient, two DW-MRI acquisitions are needed: a first one using a b-value equal to zero in order to have a reference signal without the effect of diffusion and a second one using a non-zero b-value. This will give rise to two signals: S_0 and S that we can put together to obtain the ADC using the following formula[39]:

$$ADC = -log(\frac{S}{S_0}/b)[mm^2/s] \tag{2.16}$$

2.2 DTI

The problem with the ADC is that it is a scalar. It does not give any information on the direction of the diffusion. To allow for tridimensional diffusion information of water molecules in each voxel, one needs to use tensors instead of scalars to extract the diffusion anisotropy effect from MRI. This gives rise to DTI. The 3×3 diffusion tensor $\mathbf{D}$ is a symmetric positive semi-definite tensor defined as follows:

$$\mathbf{D} = \begin{bmatrix} D_{xx} & D_{xy} & D_{xz} \\ D_{yx} & D_{yy} & D_{yz} \\ D_{zx} & D_{zy} & Dzz \end{bmatrix} \tag{2.17}$$

The signal attenuation resultant from the diffusion of the molecules is linked to the b-value and to the ADC via the following formula[39]:

$$Att = e^{-bADC} \tag{2.18}$$

The construction of this tensor requires the acquisition of at least 6 PGSE sequences in 6 different directions and a seventh acquisition with a b-value equal to zero to have a reference signal. In practice, more gradient's directions are acquired to be able to avoid having too much artefact and noise in the signal. The diffusion along the three orthogonal axes of the internal reference frame are the diagonal elements of $\mathbf{D}$. This matrix can be diagonalized to obtain useful scalar quantities characterizing the tissues.

$$\mathbf{D} = \mathbf{Q}\Lambda\mathbf{Q}^{-1}, with\Lambda = \begin{bmatrix}\lambda_1 & 0 & 0\\ 0 & \lambda_2 & 0\\ 0 & 0 & \lambda_3\end{bmatrix} \tag{2.19}$$

Mean Diffusivity (MD): It is a measure of the overall diffusivity in a voxel of the image. It is also an indication of the presence of obstacles to the diffusion. It is computed using the Trace (Tr) of the diagonalized diffusion tensor $\mathbf{D}$.

$$Tr(\mathbf{D}) = \lambda_1 + \lambda_2 + \lambda_3 \tag{2.20}$$

$$MD = \frac{Tr(\mathbf{D})}{3} = \frac{\lambda_1 + \lambda_2 + \lambda_3}{3} \tag{2.21}$$

Structures such as the CSF will present a high MD since the diffusion in it is isotropic while other structures presenting anisotropic diffusion such as WM and grey matter (GM) will present lower MD values.[39, 40] In Fig.2.15.A, it is possible to observe an MD map.

Axial Diffusivity (AD): It represents the diffusivity along the principal axis of the diffusion tensor.

$$AD = \lambda_1. \tag{2.22}$$

Radial Diffusivity (RD): It represents the diffusivity along the two other directions than the principal axis of the diffusion tensor. This metric can be seen as a measure of white matter damage as it increases when demyelination occurs.[41]

$$RD = \frac{\lambda_2 + \lambda_3}{2}. \tag{2.23}$$

Fractional Anisotropy (FA): It is a measure of the anisotropy and is computed by the following formula:

$$FA = \sqrt{\frac{3}{2}}\frac{\sqrt{(\lambda_1 - MD)^2 + (\lambda_2 - MD)^2 + (\lambda_3 - MD)^2}}{\sqrt{{\lambda_1}^2 + {\lambda_2}^2 + {\lambda_3}^2}}. \tag{2.24}$$

This metric varies between 0 and 1. A FA equal to zero means that all the eigenvalues are equal and then that the diffusion is perfectly isotropic. A value equal to 1 means that the diffusion is highly anisotropic. This metric can often be representative of WM integrity. Indeed, FA is considered an indirect measure of tissue integrity due to the fact that this metric decreases when demyelination occurs[41]. A FA map can be observed in

Fig.2.15.B, it is possible to see on it that voxels with low values of FA will appear dark on the image while it is the opposite for high values of FA. In Fig.2.15.C, an RGB-FA map can be observed: it is useful to have indications about the principal direction of diffusion in the different brain regions. These maps show the diffusion direction as red being left-right, green anterior-posterior, and blue superior-inferior[9].

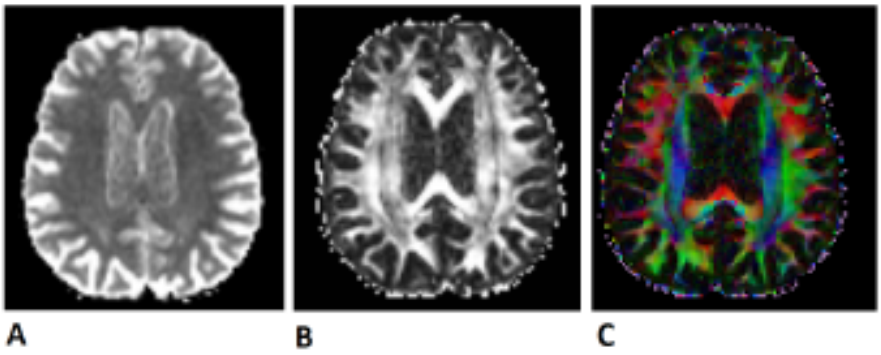

Figure 2.15: Three different maps that can be obtained using DTI. A: MD map, B: FA map, C: RGB-FA map

Limitations of DTI:

- Water molecules are expected to follow a Gaussian distribution which is not in line with reality.[40]
- Does not take into account the impact of multiple fibres that could be crossing each other in a single voxel. The result is that different structures of the brain can present the same FA value. DTI is a phenomenological and not a microstructural model. Indeed, it fits a mathematical expression to the signal with parameters that are not directly linked to the microstructures of the tissues.[42]

Advantages of DTI[42]:

- Gives global insight into brain damage and the effects of neurological pathologies.
- Easily computed.

3 Models of the brain microstructure

In the previous section, the DTI model has been described and some limitations about it have been identified. That's why more complex models of diffusion inside the brain have been developed. Three models will be presented in this section: Neurite

Orientation Dispersion and Density Imaging (NODDI)[43], DIstribution of 3D Anisotropic MicrOstructural eNvironments in Diffusion-compartment imaging (DIAMOND)[44] and Microstructure Fingerprinting (MF) [45].

3.1 NODDI

NODDI[43] is a microstructural multi-compartment model that has the vocation to link the DW-MRI signal to tissue features. Indeed, this model considers that each voxel is composed of three compartments that are related to assumptions about the underlying tissues. Unlike DTI, NODDI is then a biophysical model which can go deeper into tissue characterisation[46].

The three compartments are represented in Fig.2.16 and defined as follows:

- **Intra-cellular** (ic): Represents everything that is inside the neurite.
- **Extra-cellular** (ec): Represents the space surrounding the neurites, it is mainly composed of glial cells in healthy tissues and there is an addition of inflammatory cells in lesions.
- **CSF** (iso): Represents the space occupied by CSF.

Those three compartments are independently modelled and affect the water diffusion differently. The MR signal in each compartment is then also different and the following formula regroups the contribution of each compartment to the resulting signal:

$$A = (1 - \nu_{iso})(\nu_{ic}A_{ic} + (1 - \nu_{ic})A_{ec}) + \nu_{iso}A_{iso} \tag{2.25}$$

where A and ν are respectively the normalized signal and volume fraction for each compartment. The models used for each compartment will be described below[43].

Intra-cellular model: The intra-cellular space refers to the space inside the neurites. A neurite refers to any projection from the cell body of a neuron. This projection can be either an axon or a dendrite. The diffusion in those neurites is highly restricted due to their structure and is then almost parallel to their orientation. As the left model of Fig.2.16 shows, this compartment is represented by a set of sticks/cylinders with zero radii to capture the highly restricted diffusion perpendicularly to the neurites and the almost free diffusion along them. In practice, when applying the models to real data, a fraction called "fintra" for each voxel of the volume imaged is obtained.

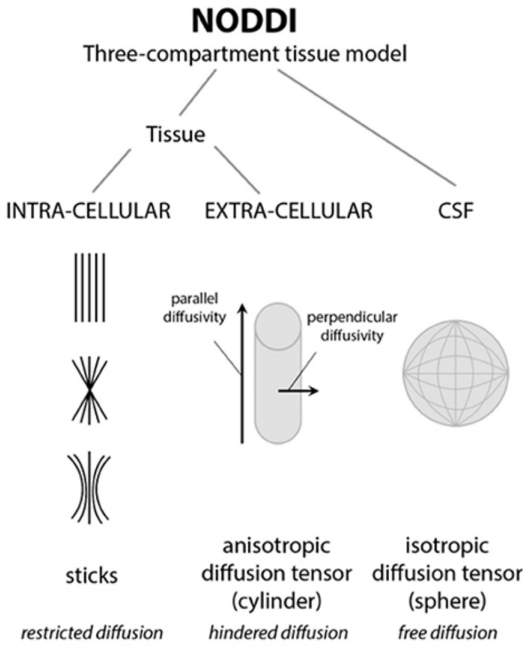

Figure 2.16: Representation of the three compartments considered in the NODDI model. From [47]

Extra-cellular model: The extra-cellular space refers to the space surrounding the neurites, composed mainly of glial cells. In this compartment, the diffusion is hindered by the presence of neurites but not restricted in a specific direction. This compartment is then modelled by a simple gaussian anisotropic diffusion. As it is represented in the centre part of Fig.2.16, the diffusion in this compartment is depicted by a cylinder with an important primary diffusion direction and a secondary one perpendicular to it which is smaller. In practice, for this model, another fraction called "fextra" for each voxel of the volume imaged is obtained.

CSF compartment: This compartment refers to the spaces where the diffusion is fully isotropic. It is therefore modelled as an isotropic gaussian diffusion which is represented by a sphere on the right part of Fig.2.16. The fraction obtained for this model is called "fiso".

Once all the parameters of the model have been estimated using typical values in vivo for the diffusivity and by fitting the model to the data using maximum likelihood estimates, the last metric can be estimated. This metric is the **Orientation Dispersion Index** (ODI). This metric ranges from 0 to 1 and locally translates the orientation dispersion of the neurites in the two first compartments. A value of one indicates that the fibres are randomly oriented while a value of 0 means that the fibres are perfectly parallel.

3.2 DIAMOND

DIAMOND is a microstructural multi-compartment model that assumes that each voxel is composed of a great number of spin packets (protons) that underwent a globally homogeneous diffusion[44]. Like NODDI, this model considers that each voxel is composed of several compartments. To put it another way, the DIAMOND model aims to arrange each voxel's spins into packets that undergo the same diffusion as Fig.2.17 shows. These voxels are composed of heterogeneous and homogeneous 3D spin packets and the diffusion of each of these spin packets is described by a diffusion tensor $\mathbf{D}$ that takes into account the characteristics of the diffusion. The contribution of each population inside a voxel to the signal is weighted by $P(\mathbf{D})$, the matrix-variate distribution that gives the fraction of the contribution of each spin packet inside a voxel. By summing the contribution of each spin packet inside a voxel, the diffusion signal S_k can be obtained:

$$S_k = S_0 \int_{\mathbf{D}} P(\mathbf{D}) e^{-b_k \mathbf{g}_k^T \mathbf{D} \mathbf{g_k}} d\mathbf{D}, \tag{2.26}$$

where S_0 is the baseline signal (b-value=0), $\mathbf{g}_k$ and b_k are the diffusion gradient direction and the b-value of volume k.

DIAMOND can be reduced to DTI if only one homogeneous population inside each voxel is considered. The diffusion tensor becomes then $\mathbf{D}_0$ and $P(\mathbf{D})$ is a delta function $\delta(\mathbf{D} - \mathbf{D}_0)$. However, considering only one compartment is not realistic. To go further, multi-tensor models (MTM) are used where the spin packets are supposed to be homogeneous and the function $P(\mathbf{D})$ that gives the fraction of the contribution of each spin packet is modelled as the sum of the delta functions corresponding to each spin packet (see Fig.2.17.B). DIAMOND goes even further to be more general by using a multivariate Gamma distribution to cancel the homogeneity hypothesis in each spin packet as shown in Fig.2.17.C. In reality, the environment is typically made up of several distinct microstructural settings, each with varying degrees of heterogeneity. That's why it is taken into account in the DIAMOND model using a matrix-variate gamma (mv-Γ) distribution defined as follows:

$$P_{\kappa,\sum}(\mathbf{D}) = \frac{|\mathbf{D}|^{\kappa - \frac{p+1}{2}}}{|\sum|^{\kappa} \Gamma_p(\kappa)} e^{-trace(\sum^{-1} \mathbf{D})}, \tag{2.27}$$

where κ is the shape parameter, $\sum$ is the scale parameter and $\Gamma_p(\kappa)$ is the multivariate Gamma function. Considering that there are N_p spin packets in a voxel, the mv-Γ distribution $P(\mathbf{D})$ can be defined by:

$$P(\mathbf{D}) = \sum_{j=1}^{N_p} f_j P_{\kappa_j,\sum_j}(\mathbf{D}), \tag{2.28}$$

where f_j represents the fraction of occupancy of each spin packet inside a voxel and ranges from 0 to 1.

As previously stated, DIAMOND is a generalized method of expressing 3D diffusion, and with a few adjustments to the direct output, new metrics like the FA, MD, and RD may also be derived. They will be referred to as cFA, cMD, cAD, and cRD in the remaining sections of this study to distinguish them from the direct DTI measures. However, unlike DTI, it also offers a broad measure of heterogeneity and takes fascicle orientations into account. One of the main limitations of this model is that this model requires the estimation of the number of different tissue compartments in each voxel.

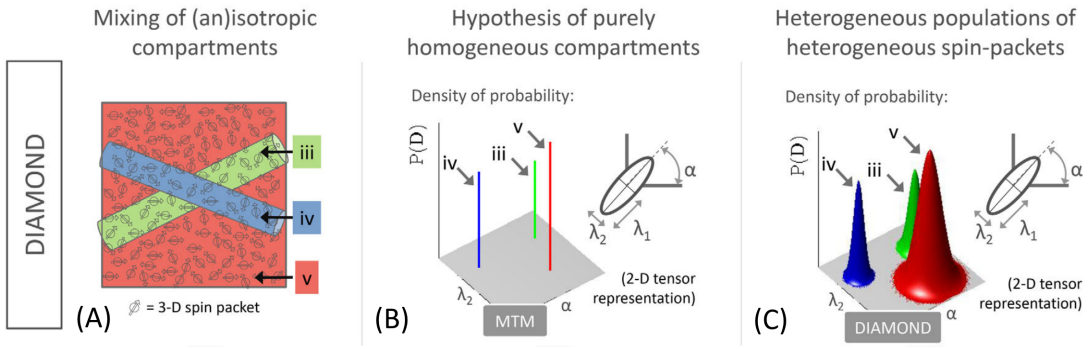

Figure 2.17: **A**: Represents three different compartments, in red an isotropic one and two anisotropic ones in blue and green. **B**: Represents the function that represents the fraction of the contribution of each spin packet for the multi-tensor model with the hypothesis of homogeneous compartments. **C**: Represents the function that represents the fraction of the contribution of each spin packet for the DIAMOND model with the hypothesis of heterogeneity inside each compartment. Adapted from [44]

3.3 MF

In the same idea as NODDI and DIAMOND, the MF model is a multicompartment model that combines Monte Carlo simulations of water molecules diffusion and the DW-MRI signal it could produce with dictionary matching to find the microstructural parameters that best describe each voxel of the input diffusion data of a patient. Like the DIAMOND model, this model is based on the superposition principle, considering that each voxel is composed of multiple structures. For example, the diffusion signal S can be represented by eq(2.29) for a WM voxel composed of K distinct fibre populations with principal unit orientations $\mathbf{u_k}$ occupying fractions v_k of this voxel and for partial volume v_{csf} of Cerebrospinal Fluid (CSF)[45].

$$S = M_0(\sum_{k=1}^{K} v_k A_{fasc}(\Omega_k, \mathbf{T_k}, \mathbf{u_k}; \mathbf{g}) + v_{csf} A_{csf}(D_{csf}, \mathbf{T_{csf}}; \mathbf{g})) \tag{2.29}$$

where M_0 is the net transverse magnetization in the concerned voxel and $A_k(\Omega_k, \mathbf{T_k}, \mathbf{u_k}; \mathbf{g})$ is the normalized DW-MRI signal of the k-th fascicle modeled by Monte Carlo simulation

for an orientation u_k, microstructural parameter Ω_k, NMR relaxation parameter T_k and gradient profile g. It is assumed a free diffusion of water in the CSF compartment (scalar D_{csf}).

The dictionary of the model is precomputed via Monte Carlo simulations and is composed of a set of *fingerprints*: $[A_{fasc}(\Omega, \mathbf{T}, \mathbf{u}; g_i)]_{i=1}^{M}$. A fingerprint is a simulated representation of a possible configuration of the microstructure inside a voxel of a certain dimension. The goal of the MF model is to use dictionary matching to find the combination of fingerprints that will best explain the input DW-MRI signal in each voxel[45]. This model will output different parameters and two important ones are the fractions of each fascicle compartment in a voxel (usually it considers 2 tissue compartments and the CSF). Next to that, there is the fibre volume fraction which is a representation of the fraction of water inside the simulated cylinders representing the tissues.[35]

3.4 The Elikopy pipeline

Elikopy is a complete diffusion MRI python processing pipeline that reduces common sources of artefacts and captures information on the brain microstructure through multiple microstructural diffusion models. One of the reasons why the Elikopy pipeline was created is to address the several DW-MRI drawbacks, which are mainly noise and artefacts. Next to that, the main goal of this python library is to make diffusion imaging easy to use for microstructural research. Indeed, integrating many processing steps makes it possible to manipulate large databases. In addition, it's structure offers a standardized framework ensuring reproducibility and consistency in the studies conducted using it. Finally, it allows to reduce error propagation and improves sensitivity [48].

To achieve the objectives cited above, this pipeline uses several python packages and proceeds in several stages[35] (As represented in Fig.2.18):

1. Audit of the data ensuring a dimension match between the images and the b-vector and b-value files along the acquisitions parameters and index files.
2. If step 1 is a success, generation of a dedicated storage folder for each subject.
3. Preprocessing is applied to the raw image to deal with the noise and artefacts. (Brain extraction, reslicing, PCA denoising, Gibbs ringing artefact correction, motion and Eddy currents distortion correction, bias field correction)
4. WM, GM and CSF masks registered on the diffusion space are obtained using a T1 image.
5. Microstructural features are obtained via the computation of the four available DW-MRI models explained in the previous sections (DTI, MF, NODDI, DIAMOND).

6. After the computation of the DW-MRI metrics, there is the possibility to register these metrics in a common space to perform region-wise, voxel-wise or cluster-wise statistics on the dataset.

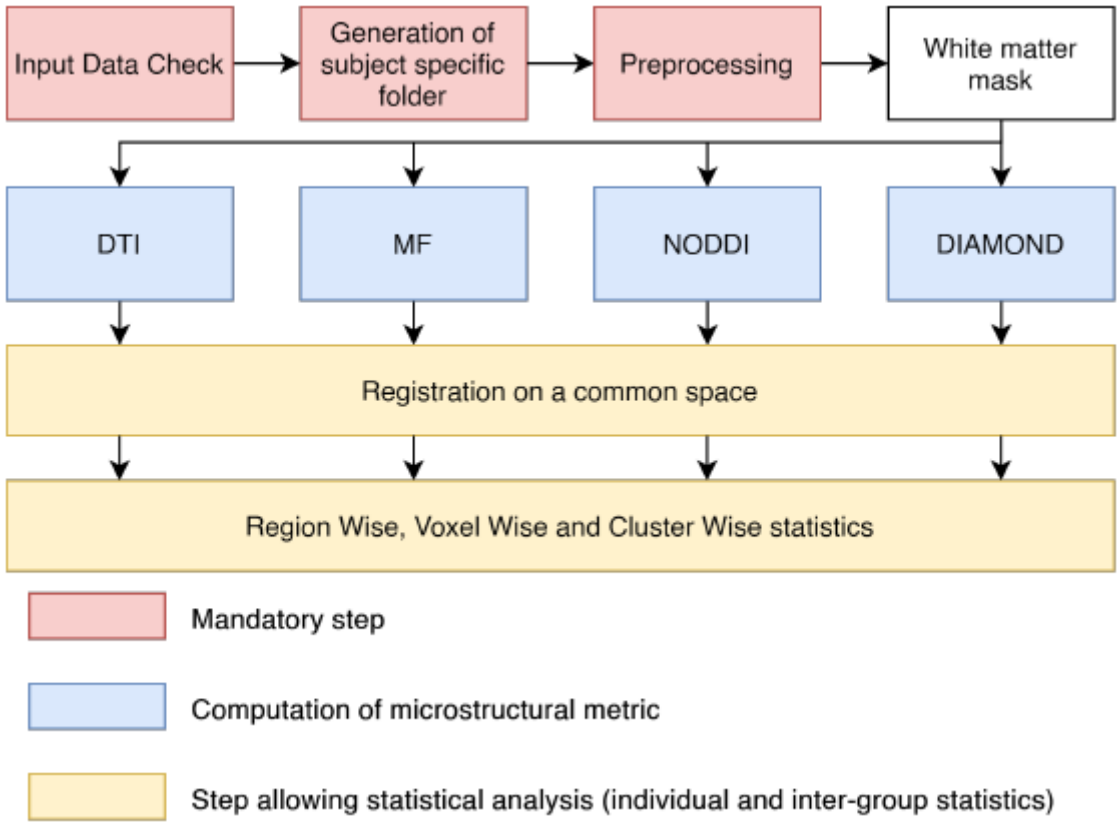

Figure 2.18: Overview of the main processing steps in the ElikoPy pipeline.[35]

4 BIDS Managing and Analysis Tool (BMAT)

4.1 Context

MRI is the go-to technique to assess brain pathologies in vivo, such as MS. However, the study of this neurological disorder often requires the acquisition of multiple MRI sequences, which results in a large set of complex data in non-standardized formats. This makes data sharing and reuse (inside or between labs) challenging, if not impossible, and makes it more complex than necessary to implement automatic pipelines. That's why a well-structured organization of neuroimaging data is required. In this framework, the Brain Imaging Data Structure (BIDS) format proposes a universal standard for naming

and organizing neuroimaging data. Adopting this format ensures an organized and homogeneous structuration of neuroimaging data and facilitates the development of automated neuroimaging tools and data sharing[3].

Simply said, a BIDS dataset's root directory contains all of the raw data transformed into an open file format, such as the Neuroimaging Informatics Technology Initiative (NIfTI) for images[49]. The storage of these converted data is realised according to the subject, session and data type, each representing a subfolder. The files are stored in the last subfolder corresponding to its data type and are named according to an explicit and specific convention following a <key-value> scheme. In the case of diffusion data for example, for subject 001 and session 01 in the BIDS dataset *BIDS_R4* it is possible to have a path like this one with the diffusion file at the end (see Fig.2.19):

BIDS_R4/sub-001/ses-01/dwi/sub-001_ses-01_acq-multishell_run-5_dwi.nii.gz

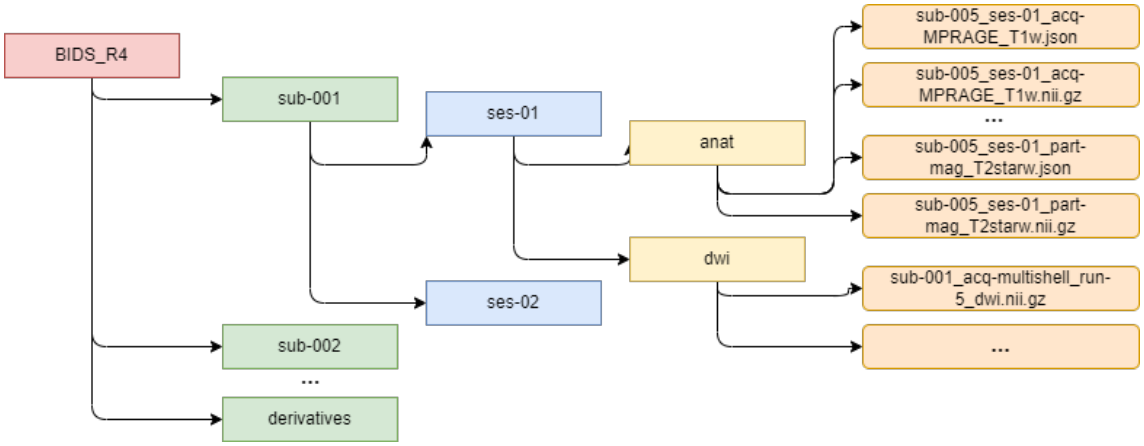

Figure 2.19: Overview of the BIDS format

The sourcedata and derivatives directories, which hold the original and the processed data, respectively, are also included in the main directory. For each image file in the dataset, a corresponding JavaScript Object Notation (JSON) file containing the metadata is attached. Moreover, the dataset also contains a general JSON file called *dataset_description.json* containing all the information about the dataset in question and a Tabular Separated Value (TSV) file called *participants.tsv* containing information about the subjects included in the dataset[3, 4].

The high number of restrictive rules needed to manage various types of neuroimaging data limits the dissemination and applicability of the BIDS format, even though it is a promising method for organizing neuroimaging datasets. Therefore, to achieve mass adoption of this format, software able to automatically implement the BIDS format is required[4, 5].

4.2 The BMAT GUI

To answer the need explained in the previous section, Colin Vanden Bulcke, a PhD student from the Institute Of NeuroScience (IONS) in which I have been integrated to do my master thesis, developed a local offline neuroimaging analysis tool. This tool called BMAT[5] is a desktop application whose primary objective is to provide researchers with a user-friendly interface to create and manage BIDS datasets. Moreover, it allows for running automated tasks on the dataset and is connected to viewing tools for results analysis.

Fig2.20 shows the main window of this application. This window is composed of different widgets allowing to do several things with the dataset. One of them displays useful information about the dataset like the number of subjects, the authors of the dataset, etc while another allows one to view and navigate the BIDS directory with the directory Tree Viewer. It is also possible to display information contained in non-image files using the Quick Viewer. Moreover, specific actions can be directly applied to the dataset like renaming or removing a subject for example. The BIDS drop-down menu situated in the upper left corner of this window provides the user with other actions like checking the validity of a BIDS directory or selecting another one. Among all the options provided by this application, the most interesting one in the framework of this master thesis is the **Pipelines drop-down menu** situated on the right of the BIDS drop-down menu. Indeed, this menu allows the user to run specific tasks on the dataset in a fully automatic way. This pipeline drop-down menu coupled with the way it has been developed allows the implementation of new pipelines[5]. In the context of this work, a brain lesions segmentation pipeline has been integrated into the BMAT software as will be explained in section 1 of chapter 3.

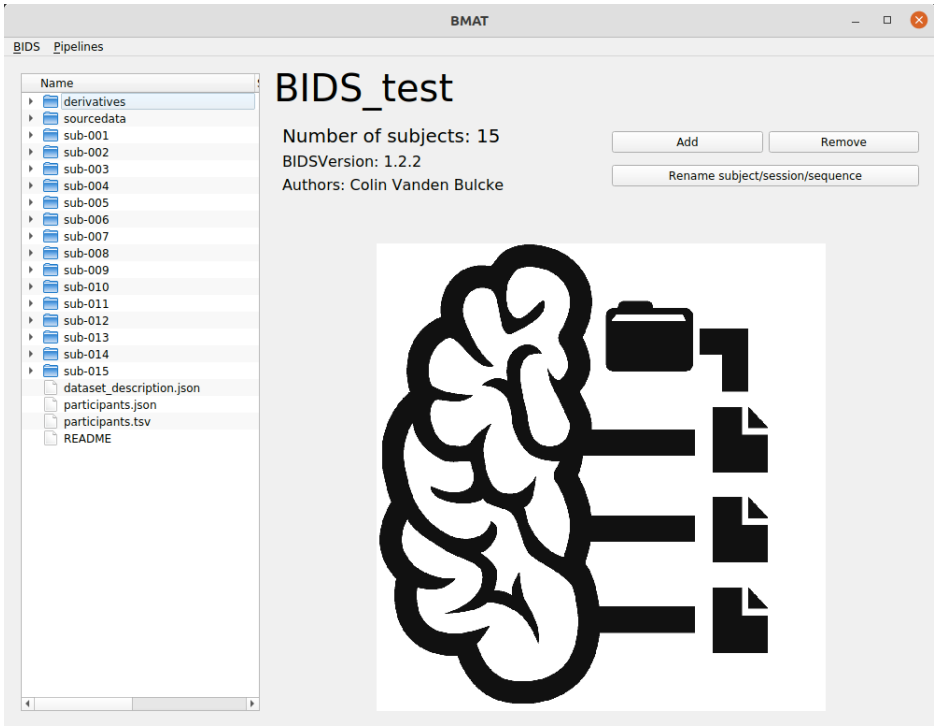

Figure 2.20: Overview of the BMAT software's main window

Part II

Microstructural analysis

Chapter 3

Method and material

1 Adaptation of a brain lesions segmentation pipeline

As explained in section 4 of chapter 2, the BMAT software provides researchers with a user-friendly interface to create and manage BIDS datasets and allows them to integrate pipelines to it for running automated tasks on the dataset. This application is of great interest because, in the domain of MS imaging, most of the developed tools are currently only accessible to technical researchers. This hinders their wider use, especially for clinicians and clinical researchers with little or no background in computer science that would want to employ them. In the framework of this master thesis, I worked on the integration of an existing brain lesion segmentation pipeline called *Les_VoLoc* to BMAT. This pipeline was written by the PhD student Maxence Wynen in 2021 as part of his master thesis. Unfortunately, it was only usable with bash commands, which hindered its wider use as explained earlier and stimulated the need to update, upgrade and translate it to python to integrate it to BMAT. The use of *Les_VoLoc* together with other pipelines already integrated into BMAT allows the study of different MS biomarkers such as PRLs, on which an extensive study using DW-MRI has also been conducted and is described in section 2 of this chapter. BMAT, with the pipelines it integrates, has been the subject of a written paper where I am the third author, submitted in a special issue about Multiple Sclerosis in Neuroimage: Clinical journal.

1.1 Technical tools

Advanced Normalization Tools (ANTs)

In this pipeline, image registration has to be done multiple times. To do so, ANTs is used. It is an open-source software library consisting of a suite of state-of-the-art image registration tools. The choice to use this tool by the previous author of this pipeline

was motivated by the fact that a recent study concludes that the ANTS registration tool provides the best registration accuracy compared to 4 other registration tools usually used by searchers[50]. Two functions of this toolkit are used daily in this work: *antsRegistrationSyNQuick* and *antsApplyTransforms*, with the first function giving as output an affine, transformed moving image toward an inputted fixed image and the transformation matrix associated with this transformation. The second function takes in argument a transformation matrix and applies it to an input image on which the transformation it contains has to be applied[51].

FreeSurfer and Sequence Adaptive Multimodal SEGmentation (SAMSEG)

FreeSurfer is an open-source neuroimaging toolkit for processing, analyzing and visualising human brain MR images. It has a lot of processing tools but in the framework of this pipeline, the interesting ones concern anatomical segmentation. Four functions of this library are used in this pipeline:

- *recon-all*: allows performing brain segmentation[52].
- *motioncor*: allows to correct for small motions and standardize the image in input with 1mm isotropic voxels and a reduced size[52].
- *run_samseg*: comes from the SAMSEG tool, which has been developed to robustly segment dozens of brain structures from head scanners and has a special extension allowing to segment white matter lesions in MS patients[53].
- *mri_convert* allows for converting different file formats[54].
- *mri_segstats*: allows computing statistics on segmented volumes[55].

1.2 Brain lesions segmentation pipeline integrated to BMAT

The first step to integrate *Les_VoLoc* to BMAT was to update it. Indeed, some of the file names and paths it used did not conform to the actual BIDS format. Once this update is finished, the upgrade and the adaptation in python can be done. The choice to translate the whole pipeline in python is motivated by the fact that the BMAT software has been developed using PyQt5, which allows creating GUI in python. Without going into the details of what changes and what does not in the pipeline, this section will make the presentation of the upgraded version of *Les_VoLoc*.

This pipeline can be viewed in two parts as represented in Fig.3.1 and described here:

- The first one going from step 1 to step 3 (described below) uses SAMSEG[53] to automatically perform segmentation of WM lesions based on the FLAIR and, if available, the MPRAGE contrasts to output a binary mask of the WM lesions.
- The second part (steps 4 to 8) uses the FreeSurfer's *recon-all* output and manipulates it with the outputs of the first part to give as output a *.csv* file containing information about the volumetry and location of the segmented lesions in the brain.

The final version of *Les_VoLoc* takes the form of a global python function taking 9 arguments in it that are tunable depending on what are the user's data and needs. All the file names in the pipeline follow the BIDS format but to ease the notations, only the important part of the names are given in the following description. The different steps of this pipeline are:

1. Depending on the computational power of the user's device, a standardization option is proposed to decrease the size of the images for step 1. If the standardization option is active, the FreeSurfer's *motioncor* function will be applied to the FLAIR image to output a standardized 255 cubed image with a reduced size. The MPRAGE image will then be registered on the standardized FLAIR image. If the standardization option is not active, the MPRAGE image is directly registered on the FLAIR image.
2. In this step, the FLAIR and MPRAGE images of the previous step are given in argument to Freesurfer's *run_samseg* which will give as output the brain lesion segmentation file called *seg.mgz* and a lesion probability mask containing the probability to be a lesion for each voxel.
3. The next step consists in binarizing the lesion probability mask according to a threshold chosen by the user to obtain the final lesion mask called *lesion_binary.nii.gz* (The value of this threshold is set to 0.5 by default but the user can change it). This step is the last step of the first part of this segmentation pipeline.
4. If the user wants to execute the second part of the pipeline, the FreeSurfer's *recon-all* function has to be executed with the MPRAGE image to obtain a file called *aseg.mgz* containing the segmentation of the whole brain.
5. In this step, registrations and transformations are applied to ensure that the *aseg.mgz* file and the *lesion_binary.nii.gz* are on the same coordinate system. This step ends up with two new files: the *lesion_fs.mgz* (lesion mask in FreeSurfer space) and *aseg_used.nii.gz* (brain segmentation in SAMSEG space).
6. This step works in the coordinate system of SAMSEG. It consists in merging the lesion segmentation with the brain segmentation to obtain information on the location of the lesions. The output file is called *aseg_lesions.nii.gz*

7. Each lesion from the file outputted in the previous step is labelled and the volume of these is computed as well as their location. The outputs of this step are a 3D labelled lesion mask and a *.csv* file containing the information computed on the lesions.

8. The last step of the pipeline consists in using FreeSurfer's *mri_segstats* function to compute brain tissue volumes and merge the outputted stats with the one in the *.csv* file of the previous step to obtain a final *Vo_Loc.csv* file similar to the one in the previous version of the pipeline[18] containing the following information:

    - Subject ID
    - Total Intracranial Volume (TIV)
    - Normalized brain volume (Original volume/TIV)
    - Normalized WM volume
    - Normalized GM volume
    - Normalized ventricles volume
    - Normalized thalamic volume
    - Normalized putamen volume
    - Normalized caudate volume
    - Normalized cerebellar GM, WM and total volume
    - Total lesional volume
    - Total number of lesions
    - Percentage of lesions per location

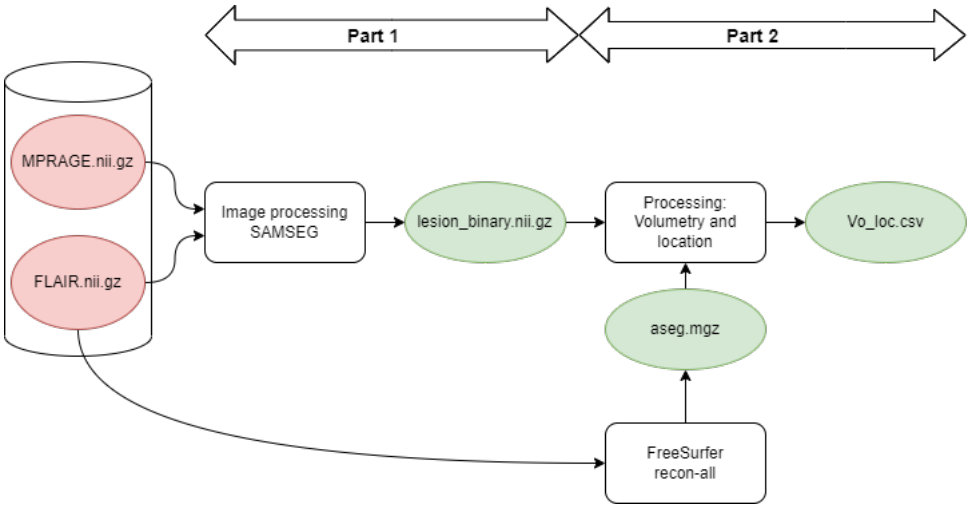

Figure 3.1: Flowchart giving a synthetic representation of the brain lesions segmentation pipeline with the two parts.

2 Microstructural analysis using DW-MRI

Next to the work done on *Les_VoLoc*, in the framework of this master thesis, I am in charge of an exploratory analysis that will be followed by a larger-scale study to be carried out by the end of 2022 with the aim of publishing a paper where I will be one of the authors. The objective is here to study the PRLs from a diffusion point of view to see whether the diffusion metrics (synthesized in Table 3.1) output by the different diffusion models can provide information or confirm the potential of PRLs to be a good prognostic biomarker. Indeed, PRLs are considered as more destructive lesions causing more axonal damage than others, thus the expectations are that the diffusion within these lesions is higher than in control lesions.

2.1 Data collection

To realize this study on the brain microstructure of MS patients, a total of 22 patients diagnosed with MS or with markers that may indicate a possible progression to MS were included in this work. These patients originated from a dataset from UCLouvain-Cliniques Universitaires Saint-Luc. The group of patients is composed of 14 females and 8 males with a mean age of 42 $\pm$ 12 years (range [22-60]). The dataset is composed of 11 RRMS, 5 SPMS, 1 PPMS, 3 CIS and 2 RIS. Images were acquired using the 3T Signa^{TM} Premier, GE Healthcare. The following sequences were acquired with an imaging frequency of $127.7Hz$: 3D-Classic T2 (TR,TE = 5317, 109.248 ms); 3D-MPRAGE_T1w (TR,TE,TI = 2187, 2.96, 900 ms); 3D-FLAIR (TR,TE,TI = 5002, 105.49, 1483 ms), 3D-MP2RAGE (TR,TE,TI = 5000, 1.98, 700 ms); 3D-T2starw (TR,TE = 80.93, 35ms); 3D-MPRAGE (TR,TE = 5000, 1.98 ms) and 3D-Diffusion multishell scans (167 volumes: 7 acquired with a null b-value and 160 with different b-values (volume number) = [1000 (64), 2000 (32), 3000 (32), 5000 (32)]s/mm^2, each volume has a shape of 110x110x68). An example of all these images can be found in appendixA.

The preprocessing and processing of the diffusion data were carried out through the ElikoPy pipeline, as described in section 3.4, to get rid of the different artefacts in the images and obtain the diffusion metrics from the different models (DTI, NODDI, MF, DIAMOND).

Image segmentation

The goal of this study is to analyse the microstructural differences between two lesion types: PRLs and control lesions. For this purpose, it was necessary to identify the lesions in each patient and segment them. All the segmentation process has been done using ITK-SNAP[56], a software used to segment structures in 3D medical images. This application provides a feature to perform manual delineation and labelling of the lesions

in 3D. An example of segmentation is shown in Fig.3.2

For PRLs, the lesion identification has been done by two searchers and doctors in neurology from the Institute Of NeuroScience (IONS): Pr. Pietro Maggi and PhD student Océane Perdaens. After the identification of the lesions on the phase image of the susceptibility-based T2*, as commonly done in the scientific community[57], they located them in ITK-SNAP using 2D patches so that Lukas Swieboda, another PhD student from their group, could perform the 3D segmentation in the application. After the PRLs segmentations were made by Lukas, they have been verified and corrected by Océane to have the most accurate segmentation possible.

Concerning the control lesions, they have been identified and located by Pietro and Oceane using 2D patches on ITK-SNAP. For each subject, they tried to find as many control lesions as PRLs. Moreover, these control lesions were searched in the contralateral white matter. Then, to have the highest accuracy in the choice of control lesions, they tried to identify discrete and non-confluent lesions. Finally, if it was too difficult for certain patients to make the distinction between PRLs and control lesions, no control lesions were patched. After the control lesions were patched, the 3D segmentation has been made.

The segmentation phases end up with 22 patients segmented with PRLs and 12 of them with control lesions. The 12 patients with both PRLs and control lesions account for 79 lesions (52 PRLs and 27 Control). With the addition of the PRLs from the 10 patients with only PRLs segmented, the final count is 173 lesions with 27 Control lesions and 146 PRLs.

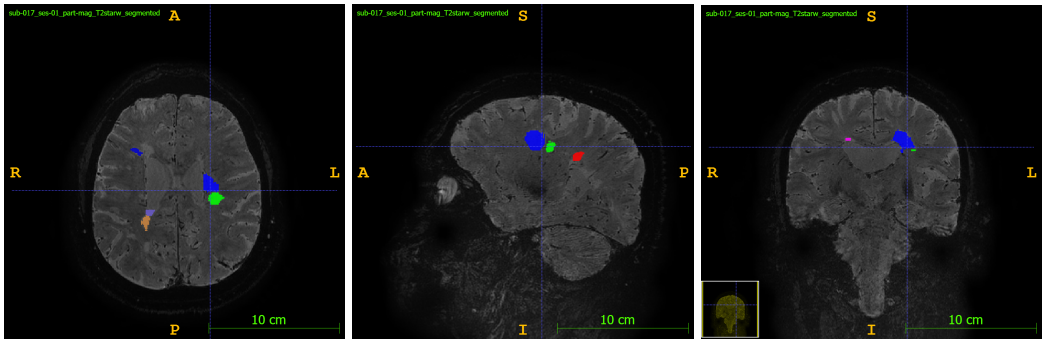

A B C

Figure 3.2: Representation of the result of a 3D segmentation of PRLs using ITK-SNAP **A**: Axial view, **B**: Coronal view, **C**: Sagittal view

Image registration

To carry out this study, different images have been acquired, each of them having its resolution in its own space. Therefore, all the images have been firstly registered in the space of the 3D T2* space, which corresponds to the image with the best resolution, using ANTs registration already described in section 1.1. The segmentation masks described above have been drawn on the FLAIR image registered in the T2* referential ($388 \times 384 \times 355$). The problem was then to be able to use the segmentation mask on the diffusion space ($68 \times 110 \times 110$) to study the diffusion parameters inside the lesions. For this purpose, one needs to see how to register these lesion masks in the diffusion space. The reason why the registration has to be made on the diffusion space is to alter the least the diffusion metric computed in the diffusion space. ElikoPy uses T1 images for the preprocessing. This results in a T1 image called $T1\_corr\_projected$ at the output of the preprocessing by ElikoPy which is already in the diffusion space. The registration strategy used is described below and in Fig.3.3:

1. Register the T2starw on the original T1w image for each subject
2. Apply the transformation matrix on the lesion masks (PRLs and cortical lesions)
3. Register the T1w image on the $T1\_corr\_projected$ to have it in the diffusion space
4. Apply the transformation matrix on the lesions masks registered in step 2

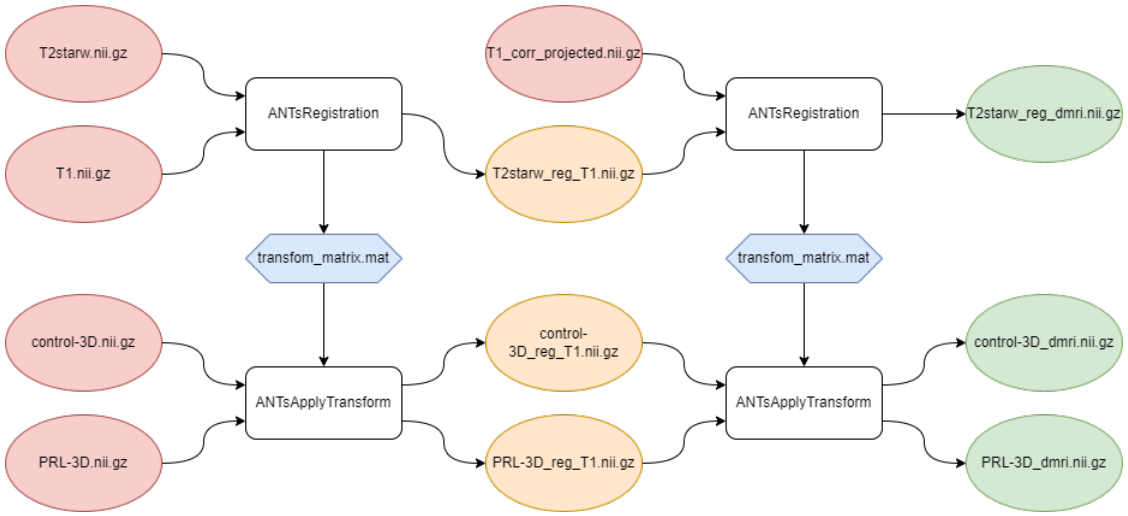

Figure 3.3: Flowchart of the registration process to obtain the final lesion masks registered on the diffusion space.

Another parameter studied in this work is the T1 value from a T1map. To study this parameter, there was no need to register in the diffusion space. What has been

done is the registration of the T1map on the T2star referential where the lesions have been segmented. To do so, one needs to use another 3D image to obtain a satisfactory registration. The 3D-UNIT1 image has been used because it has better anatomical contrast than the T1map and is in the same space. The procedure is described below:

1. Register the UNIT1 image on the T2starw for each subject
2. Apply the transformation matrix on the T1map

All the registrations were made using two different functions from the ANTs software already described in section 1.1: *antsRegistrationSyNQuick* and *antsApplyTransforms*.

2.2 Microstructural analysis

Once all patients data have been preprocessed, all lesions segmented and all lesion-masks registered, the next step was to process those data to obtain some results. To do so, a pipeline has been written using python to compute the mean of each specific metric studied inside each lesion separately. Then, means have been computed for each type of lesion and each patient. The final step was to compute the means for each metric and for each lesion type. We end up with 2 global means for each metric, one for each lesion type. It is synthesized in the following equation:

$$\mu(\mu(metric, patient(i), lesion\_type), for\ i\ in [patient\_list], lesion\_type) \tag{3.1}$$

where μ represents a mean, $patient(i)$ is the ith patient and the lesion type is PRL or Control.

Statistical analysis

This work aims at studying the possible diffusion metric variations between PRLs and control lesions to allow a better characterization of them. It is therefore important to ensure that the differences in the means of the different metrics for each type of lesion are statistically significant.

For each one of the metrics studied in this section, a preliminary Student's (t-test)[58] analysis was performed in order to highlight statistically significant metric changes in every lesion type. To this aim, a two-sided paired t-test was performed for each metric of interest. The goal of a two-sided t-test compared to a one-sided t-test is to assess whether the means for two populations (here PRLs and control lesions) are different or not while the one-sided t-test will detect an increase or a decrease between the two means.

In concrete terms, a t-score and a p-value were calculated for each metric in the following way:

$$t = \frac{(\bar{x_1} - \bar{x_2})}{s_p\sqrt{\frac{1}{n_1} + \frac{1}{n_2}}}, \text{ with and } pvalue = Pr(T \geq |t||H_0) \tag{3.2}$$

where

$$s_p^2 = \frac{((n_1 - 1){s_1}^2) + ((n_2 - 1){s_2}^2)}{n_1 + n_2 - 2}$$

The t-score is a metric characterizing the differences between the population means while the p-value represents the probability that the t-score obtained is at least as extreme as the one observed in the dataset given for the t-test. The significance level is generally set to 5%, which means for a two-sided t-test that a p-value is considered as significant if it is smaller than 2.5%. If it is the case, it means that the chances of wrongly declaring that a change is significant are lower than 5%. This criterion has been applied to each of the metrics that will be described in the rest of this section to see whether it is possible to draw conclusions about them.

The t-test is a parametric test that uses the assumption that the data are normally distributed. However, as already stated in section 2.1, control lesions were segmented according to some criteria, resulting in an unbalanced number of patients with both control and PRLs segmented compared to patients with PRLs (146 PRLs vs 27 controls). To compare the means using all available data, another statistical test has been used: a two-sided Mann-Whitney U test[59]. This test is a non-parametric equivalent to the unpaired t-test but the advantage is that it doesn't assume a normal distribution of the data. The goal is the same as the t-test, assess the fact that means are different for two populations or not. The U statistic is a metric characterizing the degree of overlap in ranks between 2 groups. For each group, a U score is calculated using the following formula:

$$U_1 = n_1 n_2 + \frac{n_1(n_1 + 1)}{2} - R_1 \tag{3.3}$$

$$U_2 = n_1 n_2 + \frac{n_2(n_2 + 1)}{2} - R_2 \tag{3.4}$$

where n_1, n_2, R_1 and R_2 represent respectively the number of data in population 1, the number of data in population 2, the rank sum for population 1 and the rank sum for population 2.

After the computation of U_1 and U_2, the minimum of these two is kept and compared to standardized tables with critical values for a certain level of significance. If $min(U_1, U_2)$ is smaller than the critical value for n_1 and n_2, then the difference between the two groups is considered significant and the null hypothesis is rejected.

To sum up the statistical methodology, a paired t-test has been computed on all the metrics for the 12 patients with both control lesions and PRLs. After that, to compare

the results of the t-test using all the available data with PRLs, a second non-parametric statistical test called the Mann-Whitney U test has been computed on all the metrics for the 24 patients.

T1map

From the 3D-MP2RAGE images acquired, a T1map has been computed for each patient to study the T1 values inside the two different types of lesions. Indeed, T1 values have been identified to be a good indicator of myelin damage with longer T1 in demyelinated than remyelinated lesions.[60, 6]

DTI

As already explained in section 2.2, the DTI model allows the computing of four different metrics (**AD, RD, MD, FA**) that are represented in Fig.3.4 and that can be studied to observe some changes in the microstructure of the brain.

Due to the nature of PRLs, it is expected to observe a higher **FA** value within the PRLs compared to control lesions if the axonal damages are more important in PRLs than other lesions. An increase of the three other metrics (**AD, RD, MD**) in PRLs compared to control lesions would also be representative of a higher diffusion and thus more important axonal damages in PRLs.

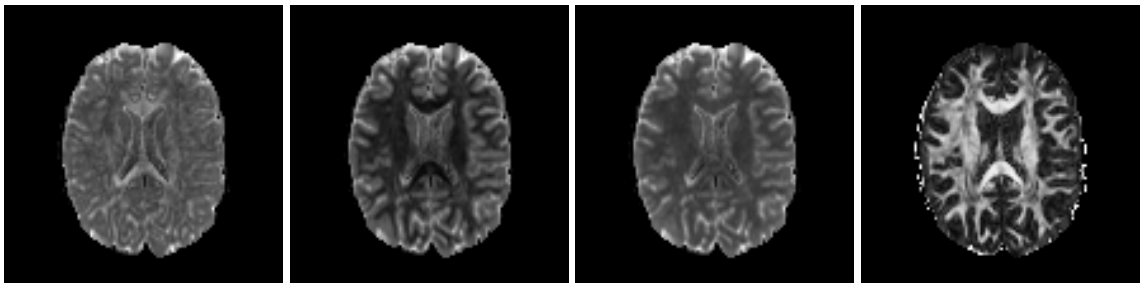

A B C D

Figure 3.4: Representation of the 4 DTI metrics. **A**: AD, **B**: RD, **C**: MD, **D**: FA

NODDI

In the same way as the DTI model, the NODDI model allows the computing of four different metrics (**fiso, fextra, fintra, ODI**) which are represented in Fig.3.5 and described in section 3.1 from chapter 2. Again, the fact that PRLs are considered more destructive than other lesions, some expectations for the changes in the values of each metric inside these lesions are expected:

- **fiso**: An increase of this metric would be representative of a diminution of the tissue fraction, meaning more axonal damages.
- **fextra**: An increase of this fraction due to the inflammatory character of PRLs causing an important presence of spherical cells (glial cells + inflammatory cells) around the axons.
- **fintra**: A decrease of this fraction due to axonal damages. As the number of axons decreases, the fraction of water inside the neurites inside a voxel also decreases.
- **ODI**: In the WM, an increase of this metric can indicate tissue rearrangement while a decrease is characteristic of axonal packing.

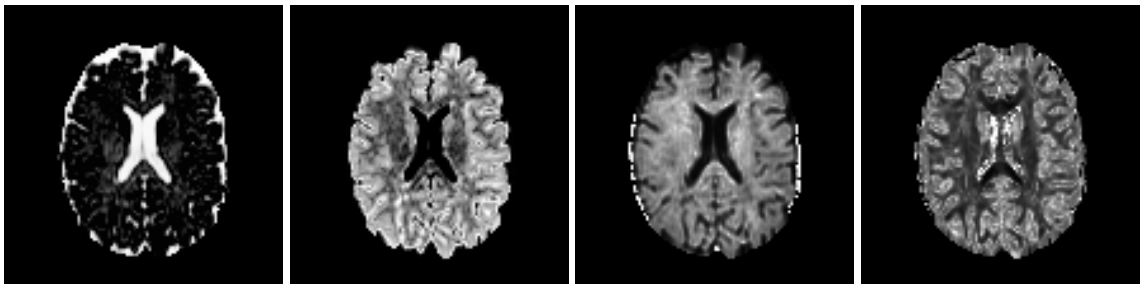

A B C D

Figure 3.5: Representation of the 4 NODDI metrics. **A**: fiso, **B**: fextra, **C**: fintra, **D**: odi

DIAMOND

In the same way as for other models, Elikopy gives as output several 3D maps with different metrics. The first interesting file is a file containing 3 fractions for each voxel. DIAMOND being a multicompartment model, the first two files correspond to the fractions of two different fibre populations ($frac\_f_0$ and $frac\_f_1$) and the third one corresponds to the fraction of CSF ($frac\_csf$) inside a voxel. As it is not easy to interpret the fraction of the fibre population, it has been decided to merge the fractions of fibre populations to obtain a new metric called $frac\_ftot$ computed with the following formula:

$$frac\_ftot = frac\_f_0 + frac\_f_1 \tag{3.5}$$

The next interesting files were files named $t0$ and $t1$, for fibre population 0 and fibre population 1, respectively. Each of them is composed of 6 values for each voxel and these values are the components of a tensor. The 6 components of this tensor allow the reconstruction of tensor $\mathbf{D}$, representing the 3D diffusion tensor from section 2.2. There are only 6 components because this tensor is a symmetric positive semi-definite tensor. From these files, a 3×3 tensor $\mathbf{D}$ is then computed for the two fibre populations in each

voxel, making it possible to compute the DTI metrics for both fibre populations thanks to the equations from section 2.2.

As there is two fibres populations, there will be DTI metrics for both fibre populations and for the CSF: ($AD(t0)$, $RD(t0)$, $MD(t0)$, $FA(t0)$, $AD(t1)$, $RD(t1)$, $MD(t1)$, $FA(t1)$, $AD(csf)$, $RD(csf)$, $MD(csf)$). For each metric, there is then one 3D map per fibre population, which is not easy to interpret. To address this limitation, it has been decided to compute new metrics that take into account the metrics from both fibre populations and from the CSF. Concerning the metrics in the CSF, the FA is supposed equal to zero due to the assumption of isotropic diffusion in this compartment. According to the litterature, the diffusivity in the CSF corresponds to 3.10^{-3}[mm^2/s][61] (then $AD(csf) = MD(csf) = RD(csf) = 3.10^{-3}$[mm^2/s]). These new weighted metrics were named wAD, wRD, wMD and wFA and are computed using the following formula:

$$wFA = \frac{frac\_f_0 * FA(t0) + frac\_f_1 * FA(t1) + frac\_csf * FA(csf)}{frac\_f_0 + frac\_f_1 + frac\_csf} \tag{3.6}$$

It is important to note that the weighted DTI metrics will have different values than the ones of the DTI model although they should be interpreted in the same way (see interpretation section 2.2). When two populations of fibres intersect, the DTI model will only consider one population in total, resulting in a signal that is the average of the two populations. If two populations are perpendicular, then the FA value will be much lower than the "real" value because the two populations are averaged together. On the contrary, by doing this weighted sum to obtain the wFA with the DIAMOND model, the value that comes out will consider both populations of fibres and it will result in a wFA value that will be closer to the "real" value that the tissues should have[62].

Again, in the same way as for other models, a list of metrics (represented in Fig.3.6) is obtained and some assumptions about their behaviour can be made:

- **wFA**: In the same way as for the DTI model, the FA value is expected to be higher within the PRLs.
- **wAD, wRD, wMD**: Again, an increase of these three metrics is waited in the PRLs compared to control lesions to represent a higher diffusion.
- **frac_ftot** and **frac_csf**: A decrease of the first one and an increase of the second one would be representative of axonal damages.

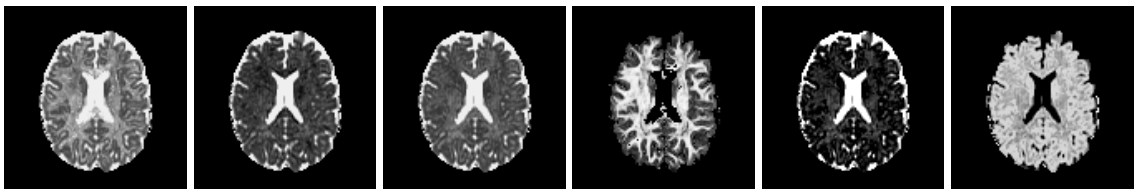

A B C D E F

Figure 3.6: Representation of the 6 DIAMOND metrics. **A**: wAD, **B**: wRD, **C**: wMD, **D**: wFA, **E**: frac_csf, **F**: frac_ftot

MF

As stated in section 3.3 from chapter 2, MF is a model that discriminates different fibre populations inside a voxel. In the case of this work, the model returns the fraction of two distinct fibre populations ($frac\_f_0$ and $frac\_f_1$) and the fraction of CSF ($frac\_csf$) inside each voxel. As for the DIAMOND model, to have something interpretable, the fractions of the two different fibre populations were merged to obtain a metric representing the total fraction of fibre inside a voxel. This metric is given by the formula:

$$frac\_ftot = frac\_f_0 + frac\_f_1 \tag{3.7}$$

The MF model also gives as output a metric called fvf stating for fibre volume fraction, this metric is also given for each fibre population and in the same way as for the fraction, a merged fibre volume fraction was computed in the following way:

$$fvf\_tot = fvf\_f_0 * frac\_f_0 + fvf\_f_1 * frac\_f_1 \tag{3.8}$$

This fvf_tot gives the fiber volume fraction inside a voxel, it means that it takes into account the volume of the entire voxel. To only take the proportion of fibres from both populations inside a voxel, it is possible to compute the last metric called the weighted fibre volume fraction with the following formula:

$$wfvf = \frac{fvf\_tot}{frac\_tot} \tag{3.9}$$

This work ends up with a list of 4 metrics for the MF model (represented in Fig.3.7) on which it is also possible to make assumptions about their changes within PRLs compared to control lesions:

- **frac_ftot** and **frac_csf**: Just like for the DIAMOND model, a decrease of the first one and an increase of the second one would be representative of axonal damage.
- **fvf_tot** and **wfvf**: Both metrics should exhibit a decrease to represent axonal damages.

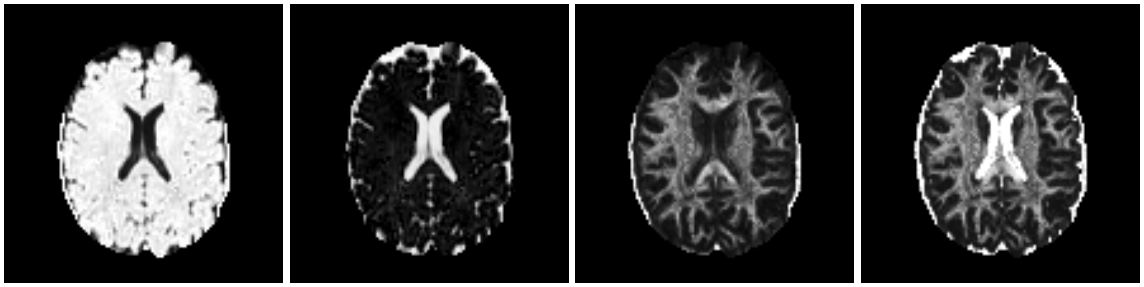

A B C D

Figure 3.7: Representation of the 4 MF metrics. **A**: frac_ftot, **B**: frac_csf, **C**: fvf_tot, **D**: wfvf

Model	Metric	Metric signification
DTI	AD	Axial Diffusivity
	RD	Radial Diffusivity
	MD	Mean Diffusivity
	FA	Fractional anisotropy
NODDI	fiso	Free water volume fraction
	fextra	Extracellular volume fraction
	fintra	Intracellular volume fraction
	odi	Fibre orientation dispersion index
DIAMOND	wAD	Weighted AD
	wRD	Weighted RD
	wMD	Weighted MD
	wFA	Weighted FA
	frac_csf	Free water fraction inside a voxel
	frac_ftot	Total tissue fraction inside a voxel
MF	frac_ftot	Total tissue fraction inside a voxel
	frac_csf	Free water fraction inside a voxel
	fvf_tot	Total fibre volume fraction (Fraction of water inside the fibers)
	wfvf	Weighted fibre volume fraction
T1map	T1 value	T1 relaxation time of a voxel

Table 3.1: Synthesis of all the metrics studied in this work to compare PRLs and control lesions.

Chapter 4

Results

1 Microstructural analysis using DW-MRI

This chapter contains the results obtained from the study explained in section 2 of chapter 3 that consists of a comparison of PRLs with control lesions using different diffusion models. These results will be described in detail and interpreted according to the theoretical information gathered in the state of the art and the expectations that have been made on the metrics changes between PRLs and control lesions.

1.1 Statistical analysis

On all the 19 metrics tested, 10 were found to be significant with the paired t-test on the 12 patients with both types of lesions and also 10 of them were found to be significant according to the unpaired U test with the addition of the 10 patients with only PRLs segmented. The choice has been made to keep the results of the significance of the Mann-Whitney U test and this decision is motivated by the fact that this test makes fewer assumptions on the properties of the dataset and also because it takes all the available data into account.

Table 4.1 makes the synthesis of the results. It is possible to observe that each of the models has at least one of its metrics that is significant, which allows interpreting results for all the models. Different levels of significance which are synthesised in Table 4.2 can be observed between metrics and even models. In the remainder of this section, all the box-plot representing the differences of means of a certain metric between PRLs and control lesions are associated with a symbol from this table to specify the level of significance of the metric represented.

Model	Metric	Means	Variation (PRL/Control)	p-value	Significant
T1map	T1 value	Control: 1214,87 PRL: 1473,9391	$+21,32\%$	$< 0,005$	**True**
DTI	AD	Control: 0,0007914 PRL: 0,0009671	$+22,21\%$	$< 0,001$	**True**
	RD	Control: 0,0004021 PRL: 0,0005246	$+30,46\%$	$< 0,001$	**True**
	MD	Control: 0,00053186 PRL: 0,00067209	$+26,37\%$	$< 0,001$	**True**
	FA	Control: 0,429575 PRL: 0,399037	$-7,11\%$	$> 0,05$	False
NODDI	fiso	Control: 0,1285 PRL: 0,1420	$+10,54\%$	$> 0,05$	False
	fextra	Control: 0,44499 PRL: 0,52922	$+18,93\%$	$< 0,01$	**True**
	fintra	Control: 0,42652 PRL: 0,32875	$-22,92\%$	$< 0,005$	**True**
	odi	Control: 0,29477 PRL: 0,25378	$-13,90\%$	$> 0,05$	False
DIAMOND	wAD	Control: 0,00184442 PRL: 0,00193283	$+4,79\%$	$> 0,05$	False
	wRD	Control: 0,00101185 PRL: 0,00120088	$+18,68\%$	$< 0,05$	**True**
	wMD	Control: 0,00128937 PRL: 0,00144486	$+12,06\%$	$> 0,05$	False
	wFA	Control: 0,6196619 PRL: 0,5179081	$-16,42\%$	$< 0,05$	**True**
	frac_csf	Control: 0,2069565 PRL: 0,266035	$+28,55\%$	$> 0,05$	False
	frac_ftot	Control: 0,7947731 PRL: 0,735179	$-7,50\%$	$> 0,05$	False
MF	frac_ftot	Control: 0,92287 PRL: 0,90333	$-2,12\%$	$> 0,05$	False
	frac_csf	Control: 0,077130 PRL: 0,09667	$+25,34\%$	$> 0,05$	False
	fvf_tot	Control: 0,252855 PRL: 0,200819	$-20,58\%$	$< 0,01$	**True**
	wfvf	Control: 0,276254 PRL: 0,226121	$-18,15\%$	$< 0,05$	**True**

Table 4.1: Table representing the principle results for the different models. For each metric (see meaning in Table 3.1), the means in both types of lesions are represented, followed by the variation between these means, the p-value and the last column synthesizes the fact that each parameter is significant or not.

p-value	Significance level	Symbol
> 0.05	Not Significant	ns
< 0.05	Significant	*
< 0.01	Highly significant	**
< 0.005	Strongly significant	***
< 0.001	Very strongly significant	****

Table 4.2: Interpretation of the p-value regarding the significance level with a symbol that is used on the box-plots to indicate this significance level.

1.2 T1map

The difference in T1 values between PRLs and control lesions is considered as strongly significant with a positive variation of 21.32% within the PRLs. This result suggests more demyelination inside the chronic active lesions with a paramagnetic rim compared to other lesions.

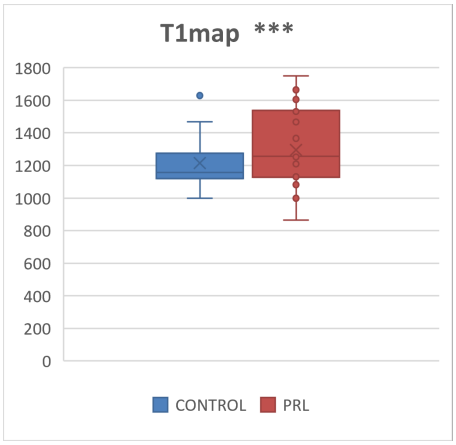

Figure 4.1: Representation of the difference of means between Control lesions and PRLs for the T1map values. ****P<0.001; ***P<0.005; **P<0.01; *P<0.05; ns = not significant.

1.3 DTI

The three metrics determined to be significant with the DTI model are the ones characterizing the diffusion of water inside a voxel. Namely: **AD**, **RD** and **MD**. AD is used to represent the diffusivity in the principal axis of the axons, RD represents the diffusivity perpendicular to the principal axis of the axonal fibres and the last one represents the global diffusivity. As it is possible to visually observe in Fig.4.2 and numerically in table

4.1, the three significant metrics are higher for PRLs compared to Control lesions (AD: $\Uparrow$ 22.21%, RD: $\Uparrow$ 30.46%, MD: $\Uparrow$ 26.37%). A closer look at table 4.1 shows that the p-values for the three metrics exhibit a very strong level of significance. The fact that all three metrics show higher values in the PRLs is representative of greater diffusion in all three directions within them, indicating more axonal damage.

Concerning the **FA** value representing the global anisotropy inside a voxel, the decrease of $7,11\%$ has not been determined as significant. However, a significant decrease would have meant more WM damage in PRLs than in control lesions since this metric is usually interpreted as an indication of WM integrity.

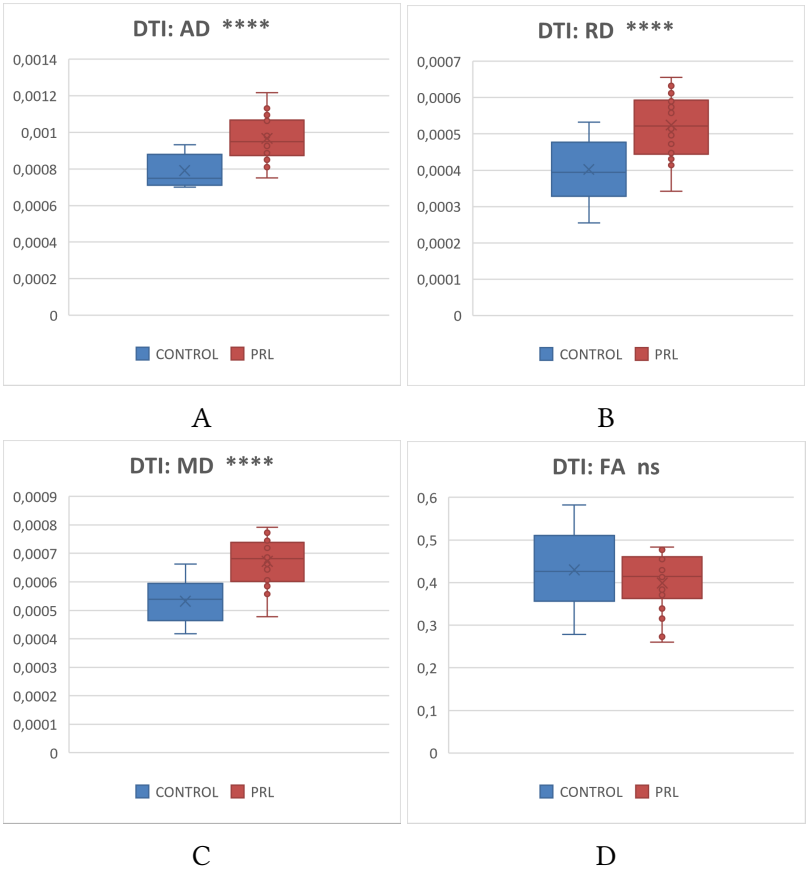

Figure 4.2: Representation of the difference of means between Control lesions and PRLs for the four metrics of the DTI model. **A**: AD, **B**: RD, **C**: MD, **D**: FA. ****P<0.001; ***P<0.005; **P<0.01; *P<0.05; ns = not significant.

1.4 NODDI

For the NODDI model, two of its four metrics are considered to be significant: **fintra** and **fextra**. The first one is called the intracellular volume fraction and can therefore be

understood as the area enclosed by the neurite membrane, which is mainly composed of water. The second one represents the fraction of space surrounding the neurites, which is composed of glial cells and in the case of intra-lesional study, more likely composed of inflammatory cells due to the inflammation. Again, it is possible to observe the variation of the metrics in both a graphical way in Fig.4.3 and in a numerical way in table 4.1.

Fintra (Fig.3.5.C) presents a high variation between PRLs and control lesions with a decrease of $22,92\%$ inside the PRLs with a p-value that ensures a strong level of significance. This lower value within PRLs can be interpreted as a lower intra-axonal volume, indicating more axonal damage.

About the second significant metric, **fextra** (Fig.3.5.B) evolves oppositely as the first one with a high increase of $18,93\%$ in PRLs compared to control lesions and a p-value ensuring a high level of significance. This result indicates a greater presence of inflammatory cells in PRLs due to the more aggressive and destructive nature of this lesion type.

The last two metrics of the NODDI model, **fiso** (Fig.3.5.A) and **odi** (3.5.D) have been determined to be insignificant. No conclusions can be made on those metrics but the variations they show are in line with the results obtained for the two significant metrics.

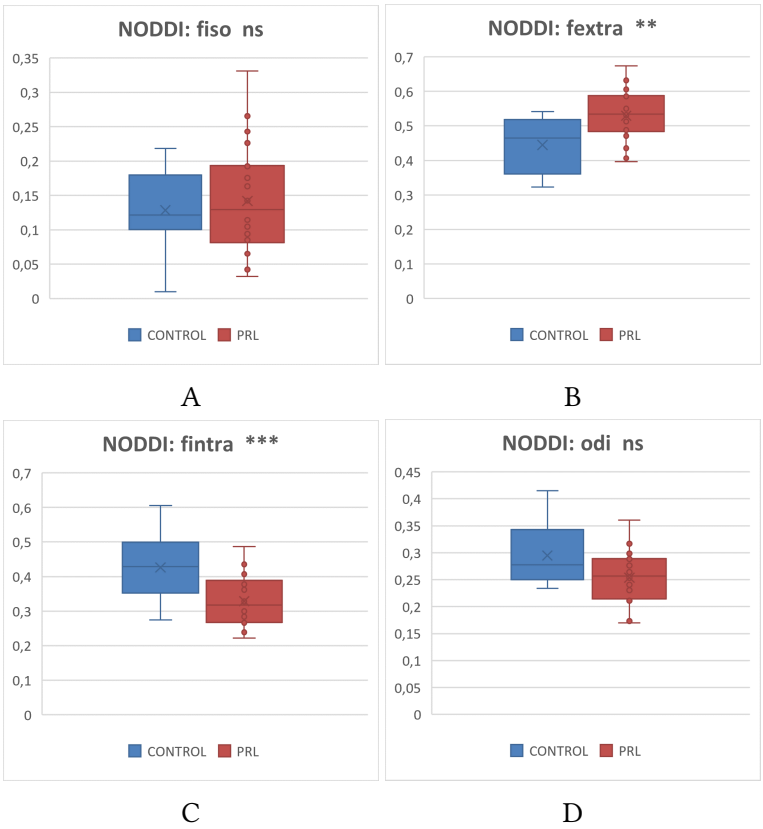

Figure 4.3: Representation of the difference of means between Control lesions and PRLs for the four metrics of the NODDI model. **A**: fiso, **B**: fextra, **C**: fintra, **D**: odi. ****P<0.001; ***P<0.005; **P<0.01; *P<0.05; ns = not significant.

1.5 DIAMOND

Two metrics of the DIAMOND model are considered significant. The first one is the **wFA** which corresponds to the fractional anisotropy inside a voxel as already stated in section 1.3. This metric is represented in Fig.4.4.D and presents a satisfactory level of significance as well as a decrease of 16.42% in PRLs compared to control lesions. As this metric is usually interpreted as an indication of WM integrity, it is possible to conclude that there is more WM damage in PRLs than in control lesions.

The second significant metric is the **wRD** which corresponds to the radial diffusivity. It's variation is represented in Fig.4.4.B and presents a satisfactory level of significance as well as an increase of 18.68% in PRLs compared to control lesions. An augmentation of this metric can be interpreted as more demyelination (see section 2.2).

The other metrics of the DIAMOND model are not considered as significant and no conclusion can be drawn from them.

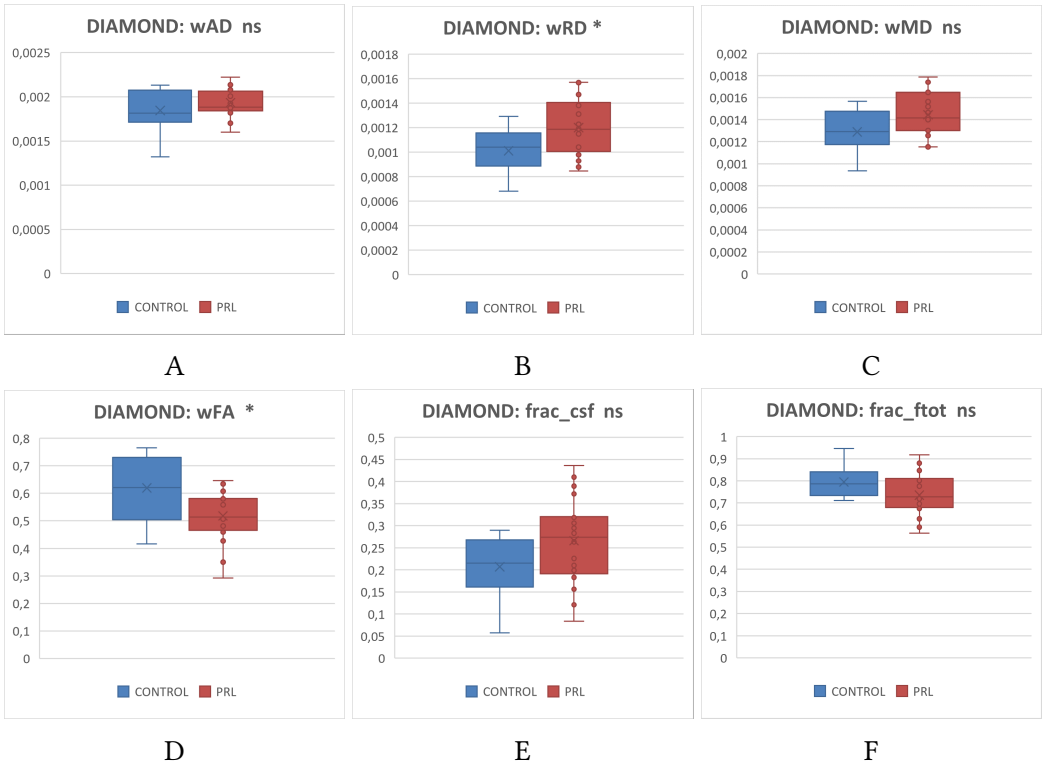

Figure 4.4: Representation of the difference of means between Control lesions and PRLs for the metrics of the DIAMOND model: **A**: wAD, **B**: wRD, **C**: wMD, **D**: wFA, **E**: frac_csf, **F**: frac_ftot. ****P<0.001; ***P<0.005; **P<0.01; *P<0.05; ns = not significant.

1.6 MF

The results of the MF models show two significant metrics: **fvf_tot** and **wfvf**. They can both be interpreted as the fraction of water inside the fibres with the first taking into account the volume of the entire voxel and the second one taking only the volume of fibres inside the voxel into account, neglecting the fraction of volume occupied by CSF.

These two metrics exhibit the same pattern of variation between PRLs and control lesions as is represented in Fig.3.7.C and Fig.3.7.D with $\Downarrow$ 20.58% and $\Downarrow$ 18.15% for **fvf_tot** and **wfvf**, respectively. A look at Table 4.1 allows observing a high level of significance for fvf_tot and a sufficient one for wfvf. Again, like the two previous models, the results of the MF model indicate more axonal damages in PRLs compared to control lesions.

The two other metrics representing the fraction of CSF and fibres inside a voxel are not considered to be significant but again, their variations are in line with the other results.

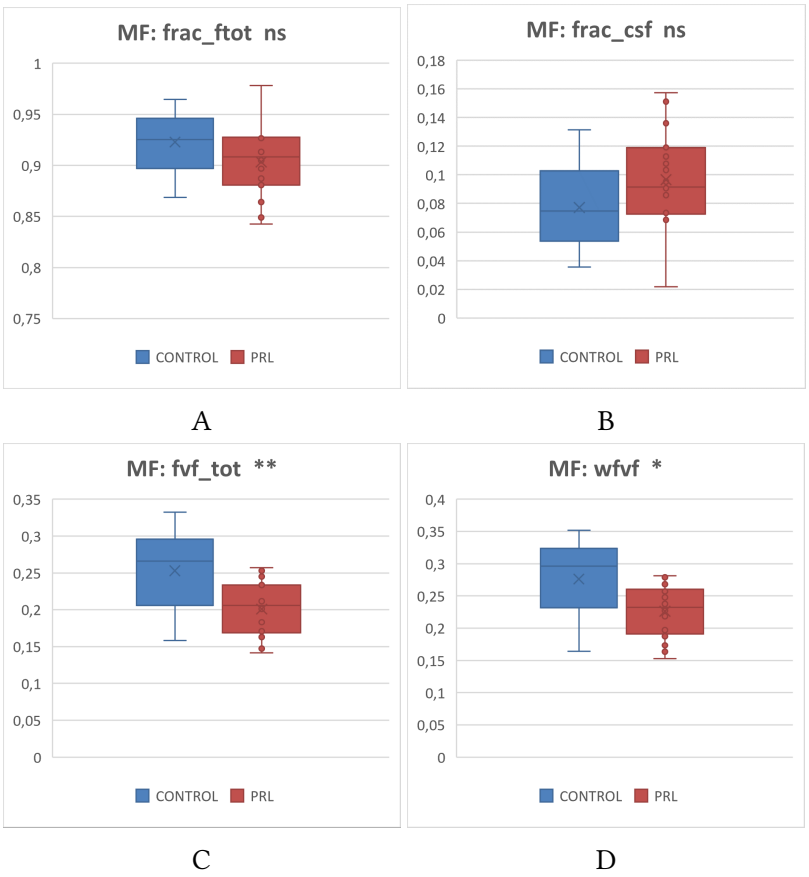

Figure 4.5: Representation of the difference of means between Control lesions and PRLs for the four metrics of the MF model. **A**: frac_ftot, **B**: frac_csf, **C**: fvf_tot, **D**: wfvf. ****P<0.001; ***P<0.005; **P<0.01; *P<0.05; ns = not significant.

Chapter 5

Discussion

1 Integration of a brain lesions segmentation pipeline to BMAT

The first part of work that has been realized in this master thesis was to update, upgrade and translate in python a brain lesions segmentation pipeline with the aim of integrating it into BMAT. BMAT is a desktop application under development in our lab whose primary objective is to provide researchers with a user-friendly interface to create and manage BIDS datasets. Moreover, it allows for running automated tasks on the dataset using various pipelines integrated into it.

With the integration of this brain lesion segmentation pipeline into the BMAT software, clinicians and researchers are now able to use this tool without the need for any background in computer science.

Lesion segmentation being a fundamental task in MS MRI studies, the integration of this tool to BMAT can help academic clinical researchers to have an automatically computed brain WM lesion mask. Specifically, the segmentation program used in this pipeline "SAMSEG" showed robust performance for WM lesion segmentation[53]. This segmentation pipeline has been included in a scientific paper presenting BMAT which is currently under peer review on a high impact international neuroimaging journal (I am the third author in the paper's author list).

Having lesion automatically segmented using BMAT can be especially useful when aiming at further characterizing WM lesions and related biomarkers, such as PRLs. With the pipeline being now integrated into BMAT, it will be easier to use it on large database for this kind of study.

2 Discussion around the different diffusion metrics variations

An additional goal of this master thesis was to characterize PRLs as compared to control brain WM lesions, using four different diffusion models and their metrics, in order to get new insight on the pathological basis of this novel MS prognostic biomarker.

The first metric studied was the lesional T1 value. This work showed that PRLs exhibit higher T1 values than control lesions, suggesting that chronic active MRI lesions have a more destructive phenotype. The results of our pilot study, conducted on a small number of patients, are in agreement with the ones of previous larger-scale studies,[6, 60] and suggest that PRLs are more demyelinated and less prone to repair.

The NODDI model also showed results consistent with the literature. One previous study[57] has shown different patterns of axon and myelin damage within different lesion types using the diffusion model NODDI. They investigated the NDI, which corresponds to the intra-axonal fraction, to characterize the profiles of axon and myelin damage in PRL. With this metric, they concluded that PRLs contain substantially lower amounts of myelin and axons than other MS lesions. The intra-axonal fraction results of our study are in line with these previous findings and confirm a more destructive phenotype for PRL vs other lesion types. Moreover, our extra axonal fraction results extend previous findings[57], by showing that PRL are also characterized by more inflammatory cells compared to non-chronic active lesions.

Concerning the MF model, the results suggest that PRLs exhibit more axonal damage than other lesions. Of note, this model has been developed recently by the UCLouvain and therefore it has not been possible to compare our results to previous already published works on MS lesions. However, by looking at the definition of the metrics, it is possible to compare our MF model results with the ones of the NODDI model. Indeed fintra and fvf_tot represent a similar parameter, the water fraction inside the cylinders representing the axons. Table 4.1 shows that these two metrics exhibit a negative variation of around $\Downarrow 20\%$ between PRLs and control lesions and a correlation test indicates a correlation of 0.84 between the two metrics, which allows concluding that our MF model results are also consistent with the ones obtained with NODDI and with the ones coming from MRI-pathological MS studies[63, 64].

Based on an article explaining how the DTI scalars relate to brain structure[65], it is possible to conclude with the DTI and DIAMOND models that PRLs exhibit more myelin and axonal damage than control lesions. The article shows that an increase in both the RD and the MD and a decrease in the FA are characteristic of demyelination and axonal

degeneration. In the framework of this master thesis, the DTI and DIAMOND models show an increase in RD within PRLs and the DTI also shows an increase in MD and AD within PRLs, suggesting more myelin and axonal damage in PRLs, which is coherent with the results obtained with the other models. The DTI model also shows a decrease in the FA but this decrease is not significant. However, the DIAMOND model shows a larger decrease of its wFA in PRLs compared to other lesions which is significant, allowing to confirm this tendency to have a decrease in the fractional anisotropy in PRLs compared to other lesions. The fact that the FA and the wFA evolve in the same way suggests that the DTI and the DIAMOND models are consistent. And the fact that the variation of the wFA is larger than the one of the FA may suggest that the DIAMOND model is a more sophisticated model that is more sensitive to microstructural changes since it takes into account fibre crossing (as already explained in section 2.2), giving a value for the fractional anisotropy that is closer to the "real one"[62].

To conclude, the most relevant finding of this research is a global augmentation of diffusion in PRLs compared to control lesions. This finding provides evidence that PRLs are associated with a more severe tissue damage in terms of axonal injury and inflammatory demyelination. All the models point in this direction. Moreover, our results extend existing knowledge from previous imaging studies by using new advanced microstructure DW-MRI models and are in agreement with evidences coming from neuropathological studies[6, 57, 60, 63, 64].

2.1 Limitations of the diffusion study on PRLs

The first limitation is probably the small sample size analyzed for this thesis. Indeed, although this prospective study reported interesting results consistent with previous findings, there were only 24 patients included with a highly unbalanced lesion count between PRLs and control lesions. For comparison, the article from Brain [57] had almost four times the number of MS patients included in its study. This low number of patients included in the study is due to the time-consuming nature of lesion segmentation, only data on those 24 patients were available at the time of the study. Adding more patients to this study as it will be done by the end of the year would probably allow obtaining more significant results to make the distinction between PRLs and control lesions. Indeed, this work only reports 3 metrics out of 19 with a p-value under 0.1%.

Another point that could limit the results of this study is the registration process. ANTs Registration has been used all along this work for convenience because it is easy to use, easily available and it is known that it is an efficient tool. However, other registration algorithms exist (like in FSL or DiPy) and it would be interesting to test some of them and compare their performance using a standardized method like the Euclidean

error for example[66]. Moreover, the assessment of the registration in this study was done visually, leaving room for possible inaccuracies. These inaccuracies coupled with a possible inter-rater variability in the lesions segmentation process are possible causes of deviation from reality.

The last limitation that has to be noted concerns the NODDI model. Indeed, this model is constrained by the assumption of a fixed diffusivity for each voxel in the brain tissue and the failure to account for crossing fascicles. A new model overcoming these limitations is called Multi-shell multi-tissue constrained spherical deconvolution (MSMT-CSD)[67, 68]. MSMT-CSD is a kind of evolution of the NODDI model, the latter being untouched since about 2015. MSMT-CSD can produce more reliable WM/GM/CSF volume fractions and in the large-scale study, it will be this model that will be used. However, using the NODDI is still interesting in order to compare the results with recent studies that still use this model.

3 Future perspectives

As already said, the study related to diffusion is a prospective study aiming to serve as a base for a large-scale study. Due to the limited time to realize this master thesis, only a comparison between PRLs and control lesions has been done. However, DW-MRI and all the diffusion metrics coming from it can be used to make other analyses than this one. The article from which the results of the NODDI model have been confirmed provides a good starting point to study MS with diffusion models[57].

Some ideas for the large-scale study can be listed here:

1. Study diffusion metrics in distinct MS lesion types
    - Compare diffusion metrics in WM lesions to normal-appearing white matter (NAWM) and WM of healthy controls WM-HC).
    - Compare diffusion metrics in CLs to NAGM and GM-HC.
    - Compare diffusion metrics between periventricular and juxtacortical lesions.
2. Study diffusion metrics in peri-plaque tissue around lesions
3. Study diffusion metrics in the normal-appearing brain tissue
    - Test difference NAWM and WM-HC volume-wise and voxel-wise to see if some clusters of voxels show significant differences.
    - Same for NAGM.

4. Study diffusion metrics in lesions for different MS types.
5. All the diffusion metrics can also be used to conduct longitudinal studies to see for example if some of them could provide more specific markers of white matter integrity than conventional MRI for patients recently diagnosed with RRMS.
6. Use the statistical analysis of Elikopy that can provide region-wise, voxel-wise and cluster-wise statistics.
7. *Les_VoLoc* could be used to obtain lesion masks and brain segmentation (WM, GM, NAWM, etc.) to study the different diffusion metrics in it.

Chapter 6

Conclusion

This master thesis had two main goals.

The first one was to integrate a brain lesions segmentation pipeline called *Les_VoLoc* to BMAT, a desktop application providing researchers with a user-friendly interface to create and manage BIDS datasets as well as the possibility to run automated tasks on these datasets using various processing pipelines integrated to it. To integrate this segmentation pipeline, it was necessary to update it to be conform with the actual version of the BIDS format. Then, some options were added to it and finally, it was translated into python to be compatible with BMAT. *Les_VoLoc* allows to calculate the different brain volumes of interest, segment WM lesions, compute their volumes and localize them by using various processing tools. Researchers are now able to use the information it gives in the context of large studies without the need for a background in computer science to use it since it is integrated into BMAT. Moreover, this pipeline can be used in combination with others already integrated into the application to study MRI biomarkers like PRLs. This has been the subject of a written paper currently under revision in which I am the third author.

Next to that, recent studies have pointed out the fact that it is important to study new biomarkers of MS with the aim of having a better estimation of disease prognosis. Indeed, MRI techniques currently used in the clinic only show a moderate correlation to clinical activity, limiting their prognostic relevance. With this aim, this master thesis presented a study of PRLs with a diffusion point of view. The goal was to assess the destructive nature of PRLs compared to other MS lesions using DW-MRI. To do so, four microstructural models of diffusion (DTI, NODDI, DIAMOND, MF) were used to quantify various parameters and highlight the differences between PRLs and control lesions. Each model has its specificities in the way it calculates its parameters and the assumptions it makes. When used together, all of their output metrics can be studied to formulate hypotheses on the microstructural changes that occur in PRLs compared to control lesions. The firsts steps of this study were to obtain the diffusion metrics output by the different models. It was done via the ElikoPy pipeline after having pre-processed the data. Finally,

all the metrics were studied inside the two lesion types to detect if any differences were apparent. With the help of the different metrics and their interpretation, we were finally able to confirm differences at the microstructural level between PRLs and control lesions. The most relevant finding of this research is a global augmentation of diffusion in PRLs compared to control lesions. This finding provides evidence that PRLs are associated with a more severe tissue damage in terms of axonal injury and inflammatory demyelination.

Even if some limitations are to take into account in the interpretation of the results like the low amount of data and possible inaccuracies in the registration and segmentation process, it has to be noted that our results are consistent with existing knowledge from previous imaging studies. Moreover, this work is only a prospective study that will serve as a base for a large-scale study that will be carried out by the end of 2022. In this large-scale study, there will be more than a simple comparison between two types of lesions. This master thesis will have confirmed what has already been shown about PRLs as well as give an interpretation of the different diffusion metrics.

Bibliography

[1] *Multiple sclerosis - Symptoms and causes*. Mayo Clinic. URL: https://www.mayoclinic.org/diseases-conditions/multiple-sclerosis/symptoms-causes/syc-20350269 (visited on 08/11/2022).

[2] Francesco La Rosa et al. "Cortical lesions, central vein sign, and paramagnetic rim lesions in multiple sclerosis: emerging machine learning techniques and future avenues". In: (), p. 30.

[3] Krzysztof J. Gorgolewski et al. "The brain imaging data structure, a format for organizing and describing outputs of neuroimaging experiments". In: *Scientific Data* 3.1 (June 21, 2016). Number: 1 Publisher: Nature Publishing Group, p. 160044. ISSN: 2052-4463. DOI: 10.1038/sdata.2016.44. URL: https://www.nature.com/articles/sdata201644 (visited on 08/09/2022).

[4] Krzysztof J. Gorgolewski et al. "BIDS apps: Improving ease of use, accessibility, and reproducibility of neuroimaging data analysis methods". In: *PLOS Computational Biology* 13.3 (Mar. 9, 2017). Publisher: Public Library of Science, e1005209. ISSN: 1553-7358. DOI: 10.1371/journal.pcbi.1005209. URL: https://journals.plos.org/ploscompbiol/article?id=10.1371/journal.pcbi.1005209 (visited on 08/09/2022).

[5] Colin Vanden Bulcke et al. "BMAT: an open-source BIDS Managing and Analysis Tool". In: *NeuroImage: Clinical (under revision)* (2022). URL: https://track.authorhub.elsevier.com/?uuid=56534715-d3c6-4f37-9eb6-1323c8c91e4e (visited on 08/10/2022).

[6] Martina Absinta et al. "Association of Chronic Active Multiple Sclerosis Lesions With Disability In Vivo". In: *JAMA Neurology* 76.12 (Dec. 1, 2019), p. 1474. ISSN: 2168-6149. DOI: 10.1001/jamaneurol.2019.2399. URL: https://jamanetwork.com/journals/jamaneurology/fullarticle/2747565 (visited on 07/08/2022).

[7] Pietro Maggi et al. "Chronic White Matter Inflammation and Serum Neurofilament Levels in Multiple Sclerosis". In: *Neurology* 97.6 (Aug. 10, 2021). Publisher: Wolters Kluwer Health, Inc. on behalf of the American Academy of Neurology Section: Research Article, e543–e553. ISSN: 0028-3878, 1526-632X. DOI: 10.1212/WNL.

0000000000012326. URL: https://n.neurology.org/content/97/6/e543 (visited on 07/09/2022).

[8] Pietro Maggi et al. "Paramagnetic Rim Lesions are Specific to Multiple Sclerosis: An International Multicenter 3T MRI Study". In: *Annals of Neurology* 88.5 (2020). _eprint: https://onlinelibrary.wiley.com/doi/pdf/10.1002/ana.25877, pp. 1034–1042. ISSN: 1531-8249. DOI: 10.1002/ana.25877. URL: https://onlinelibrary.wiley.com/doi/abs/10.1002/ana.25877 (visited on 07/09/2022).

[9] T.A.G.M. Huisman. "Diffusion-weighted and diffusion tensor imaging of the brain, made easy". In: *Cancer Imaging* 10.1 (Oct. 4, 2010), S163–S171. ISSN: 1740-5025. DOI: 10.1102/1470-7330.2010.9023. URL: https://www.ncbi.nlm.nih.gov/pmc/articles/PMC2967146/ (visited on 07/12/2022).

[10] *Myelin Sheath: What It Is, Purpose & Function*. Cleveland Clinic. URL: https://my.clevelandclinic.org/health/body/22974-myelin-sheath (visited on 08/11/2022).

[11] Daniel S. Reich, Claudia F. Lucchinetti, and Peter A. Calabresi. "Multiple Sclerosis". In: *New England Journal of Medicine* 378.2 (Jan. 11, 2018). Ed. by Dan L. Longo, pp. 169–180. ISSN: 0028-4793, 1533-4406. DOI: 10.1056/NEJMra1401483. URL: http://www.nejm.org/doi/10.1056/NEJMra1401483 (visited on 06/25/2022).

[12] Osmose. *Multiple sclerosis - causes, symptoms, diagnosis, treatment, pathology*. Mar. 22, 2017. URL: https://www.youtube.com/watch?v=yzH8ul5PSZ8 (visited on 07/12/2022).

[13] Kjetil Bjornevik et al. "Longitudinal analysis reveals high prevalence of Epstein-Barr virus associated with multiple sclerosis". In: *Science* 375.6578 (Jan. 21, 2022). Publisher: American Association for the Advancement of Science, pp. 296–301. DOI: 10.1126/science.abj8222. URL: https://www.science.org/doi/10.1126/science.abj8222 (visited on 08/16/2022).

[14] *MS Types*. URL: https://my-ms.org/ms_types.htm# (visited on 06/25/2022).

[15] *Types of MS | Multiple Sclerosis Society UK*. URL: https://www.mssociety.org.uk/about-ms/types-of-ms (visited on 07/12/2022).

[16] Daniel S. Reich, Claudia F. Lucchinetti, and Peter A. Calabresi. "Multiple Sclerosis". In: *New England Journal of Medicine* 378.2 (Jan. 11, 2018). Publisher: Massachusetts Medical Society _eprint: https://doi.org/10.1056/NEJMra1401483, pp. 169–180. ISSN: 0028-4793. DOI: 10.1056/NEJMra1401483. URL: https://doi.org/10.1056/NEJMra1401483 (visited on 08/18/2022).

[17] Vlad Eugen Tiu et al. “Predictive MRI Biomarkers in MS—A Critical Review”. In: *Medicina* 58.3 (Mar. 3, 2022), p. 377. ISSN: 1010-660X. DOI: 10.3390/medicina58030377. URL: https://www.ncbi.nlm.nih.gov/pmc/articles/PMC8949449/ (visited on 08/16/2022).

[18] Maxence Wynen. “Towards the integration of advanced magnetic resonance imaging biomarkers in multiple sclerosis clinical practice”. PhD thesis. 2021.

[19] Hang Zhang et al. “QSMRim-Net: Imbalance-aware learning for identification of chronic active multiple sclerosis lesions on quantitative susceptibility maps”. In: *NeuroImage: Clinical* 34 (Jan. 1, 2022), p. 102979. ISSN: 2213-1582. DOI: 10.1016/j.nicl.2022.102979. URL: https://www.sciencedirect.com/science/article/pii/S2213158222000444 (visited on 07/08/2022).

[20] Massimo Filippi et al. “Assessment of lesions on magnetic resonance imaging in multiple sclerosis: practical guidelines”. In: *Brain* 142.7 (July 1, 2019), pp. 1858–1875. ISSN: 0006-8950. DOI: 10.1093/brain/awz144. URL: https://doi.org/10.1093/brain/awz144 (visited on 07/11/2022).

[21] J. J. G. Geurts et al. “Consensus recommendations for MS cortical lesion scoring using double inversion recovery MRI”. In: *Neurology* 76.5 (Feb. 1, 2011). Publisher: Wolters Kluwer Health, Inc. on behalf of the American Academy of Neurology Section: Articles, pp. 418–424. ISSN: 0028-3878, 1526-632X. DOI: 10.1212/WNL.0b013e31820a0cc4. URL: https://n.neurology.org/content/76/5/418 (visited on 07/11/2022).

[22] D. Kidd et al. “Cortical lesions in multiple sclerosis”. In: *Brain* 122.1 (Jan. 1, 1999), pp. 17–26. ISSN: 0006-8950. DOI: 10.1093/brain/122.1.17. URL: https://doi.org/10.1093/brain/122.1.17 (visited on 07/11/2022).

[23] Massimiliano Calabrese et al. “Cortical lesion load associates with progression of disability in multiple sclerosis”. In: *Brain* 135.10 (Oct. 1, 2012), pp. 2952–2961. ISSN: 0006-8950. DOI: 10.1093/brain/aws246. URL: https://doi.org/10.1093/brain/aws246 (visited on 07/11/2022).

[24] Constantina A. Treaba et al. “Longitudinal Characterization of Cortical Lesion Development and Evolution in Multiple Sclerosis with 7.0-T MRI”. In: *Radiology* 291.3 (June 2019), pp. 740–749. ISSN: 1527-1315. DOI: 10.1148/radiol.2019181719.

[25] Andreas Junker et al. “Extensive subpial cortical demyelination is specific to multiple sclerosis”. In: *Brain Pathology* 30.3 (2020). _eprint: https://onlinelibrary.wiley.com/doi/pdf/10.1111/ pp. 641–652. ISSN: 1750-3639. DOI: 10.1111/bpa.12813. URL: https://onlinelibrary.wiley.com/doi/abs/10.1111/bpa.12813 (visited on 07/11/2022).

[26] UCL/SGSI. *Introduction aux neurosciences*. UCLCatalogue des formations 2021-2022. Publisher: UCL/ADEF. July 14, 2022. URL: https://uclouvain.be/cours-2021-lgbio1115 (visited on 07/14/2022).

[27] *History of magnetic resonance imaging*. In: *Wikipedia*. Page Version ID: 1102360329. Aug. 4, 2022. URL: https://en.wikipedia.org/w/index.php?title=History_of_magnetic_resonance_imaging&oldid=1102360329 (visited on 08/10/2022).

[28] B Kastler et al. *Comprendre l'IRM*. OCLC: 1026755244. Elsevier Masson, 2011.

[29] *Electron Spin*. Chemistry LibreTexts. Oct. 2, 2013. URL: https://chem.libretexts.org/Bookshelves/Physical_and_Theoretical_Chemistry_Textbook_Maps/Supplemental_Modules_(Physical_and_Theoretical_Chemistry)/Quantum_Mechanics/09._The_Hydrogen_Atom/Atomic_Theory/Electrons_in_Atoms/Electron_Spin (visited on 08/10/2022).

[30] *Net magnetization in MRI*. IMAIOS. URL: https://www.imaios.com/en/e-Courses/e-MRI/NMR/Net-magnetization (visited on 05/22/2022).

[31] Jeremy Jones. *Larmor frequency | Radiology Reference Article | Radiopaedia.org*. Radiopaedia. DOI: 10.53347/rID-5855. URL: https://radiopaedia.org/articles/larmor-frequency (visited on 08/10/2022).

[32] Simone Bosshard. "Non-invasive assessment of sensory and nociceptive processing in mice using functional MRI". In: (Jan. 1, 2011). DOI: 10.5167/uzh-58943.

[33] *Bloch equations*. In: *Wikipedia*. Page Version ID: 1088486612. May 18, 2022. URL: https://en.wikipedia.org/w/index.php?title=Bloch_equations&oldid=1088486612 (visited on 06/20/2022).

[34] *Magnetic field homogeneity | Radiology Reference Article | Radiopaedia.org*. URL: https://radiopaedia.org/articles/magnetic-field-homogeneity?lang=us (visited on 07/14/2022).

[35] Quentin Dessain and Mathieu Simon. "Development of an image processing pipeline for large-scale in vivo population studies of the brain microstructure". PhD thesis. 2021.

[36] Macq Benoît UCL/SGSI Kerckhofs Greet. *Medical Imaging*. UCLCatalogue des formations 2021-2022. Publisher: UCL/ADEF. July 14, 2022. URL: https://uclouvain.be/cours-2021-lgbio2050 (visited on 07/14/2022).

[37] *Diffusion MRI - 2nd Edition*. URL: https://www.elsevier.com/books/diffusion-mri/johansen-berg/978-0-12-396460-1 (visited on 07/12/2022).

[38] *Inferring Axon Diameter Sizes using Monte Carlo Simulations of Magnetic Resonance Oscillating Gradient Spin Echo Sequences ME Mercredi 1, TJ Vincent 2,3, - ppt download*. URL: https://slideplayer.com/slide/4663152/ (visited on 07/12/2022).

[39] Denis Le Bihan et al. “Diffusion tensor imaging: Concepts and applications”. In: *Journal of Magnetic Resonance Imaging* 13.4 (2001). _eprint: https://onlinelibrary.wiley.com/doi/pdf/10. pp. 534–546. ISSN: 1522-2586. DOI: 10.1002/jmri.1076. URL: https://onlinelibrary.wiley.com/doi/abs/10.1002/jmri.1076 (visited on 07/13/2022).

[40] Lauren J. O’Donnell and Carl-Fredrik Westin. “An introduction to diffusion tensor image analysis”. In: *Neurosurgery Clinics of North America* 22.2 (Apr. 2011), pp. 185–196, viii. ISSN: 1558-1349. DOI: 10.1016/j.nec.2010.12.004.

[41] Eleftherios Garyfallidis et al. “Dipy, a library for the analysis of diffusion MRI data”. In: *Frontiers in Neuroinformatics* 8 (2014). ISSN: 1662-5196. URL: https://www.frontiersin.org/articles/10.3389/fninf.2014.00008 (visited on 08/03/2022).

[42] *Table 2 . Advantages and Limitations of DTI*. ResearchGate. URL: https://www.researchgate.net/figure/Advantages-and-Limitations-of-DTI_tbl2_319558026 (visited on 08/10/2022).

[43] Hui Zhang et al. “NODDI: practical in vivo neurite orientation dispersion and density imaging of the human brain”. In: *NeuroImage* 61.4 (July 16, 2012), pp. 1000–1016. ISSN: 1095-9572. DOI: 10.1016/j.neuroimage.2012.03.072.

[44] Benoit Scherrer et al. “Characterizing brain tissue by assessment of the distribution of anisotropic microstructural environments in diffusion-compartment imaging (DIAMOND)”. In: *Magnetic Resonance in Medicine* 76.3 (Sept. 2016), pp. 963–977. ISSN: 1522-2594. DOI: 10.1002/mrm.25912.

[45] Gaëtan Rensonnet et al. “Towards microstructure fingerprinting: Estimation of tissue properties from a dictionary of Monte Carlo diffusion MRI simulations”. In: *NeuroImage* 184 (Jan. 1, 2019), pp. 964–980. ISSN: 1095-9572. DOI: 10.1016/j.neuroimage.2018.09.076.

[46] Kouhei Kamiya, Masaaki Hori, and Shigeki Aoki. “NODDI in clinical research”. In: *Journal of Neuroscience Methods* 346 (Dec. 1, 2020), p. 108908. ISSN: 1872-678X. DOI: 10.1016/j.jneumeth.2020.108908.

[47] Andrew W. Barritt et al. “Emerging Magnetic Resonance Imaging Techniques and Analysis Methods in Amyotrophic Lateral Sclerosis”. In: *Frontiers in Neurology* 9 (2018). ISSN: 1664-2295. URL: https://www.frontiersin.org/articles/10.3389/fneur.2018.01065 (visited on 07/13/2022).

[48] *Introduction to ElikoPy — ElikoPy documentation*. URL: https://elikopy.readthedocs.io/en/latest/introduction.html (visited on 08/08/2022).

[49] dfwg. *NIfTI: — Neuroimaging Informatics Technology Initiative*. URL: https://nifti.nimh.nih.gov/ (visited on 08/11/2022).

[50] Abdullah Nazib et al. *Performance of Image Registration Tools on High-Resolution 3D Brain Images*. July 13, 2018. DOI: 10.48550/arXiv.1807.04917. arXiv: 1807.04917[cs]. URL: http://arxiv.org/abs/1807.04917 (visited on 08/09/2022).

[51] Brian B Avants, Nick Tustison, and Hans Johnson. "Advanced Normalization Tools (ANTS)". In: (), p. 41.

[52] *recon-all - Free Surfer Wiki*. URL: https://surfer.nmr.mgh.harvard.edu/fswiki/recon-all#References (visited on 08/09/2022).

[53] Stefano Cerri et al. "A contrast-adaptive method for simultaneous whole-brain and lesion segmentation in multiple sclerosis". In: *NeuroImage* 225 (Jan. 15, 2021), p. 117471. ISSN: 1053-8119. DOI: 10.1016/j.neuroimage.2020.117471. URL: https://www.sciencedirect.com/science/article/pii/S1053811920309563 (visited on 08/09/2022).

[54] *mri_convert - Free Surfer Wiki*. URL: https://surfer.nmr.mgh.harvard.edu/fswiki/mri_convert (visited on 08/09/2022).

[55] *mri_segstats - Free Surfer Wiki*. URL: https://surfer.nmr.mgh.harvard.edu/fswiki/mri_segstats (visited on 08/09/2022).

[56] *ITK-SNAP Home*. URL: http://www.itksnap.org/pmwiki/pmwiki.php (visited on 07/26/2022).

[57] Reza Rahmanzadeh et al. "Myelin and axon pathology in multiple sclerosis assessed by myelin water and multi-shell diffusion imaging". In: *Brain* 144.6 (July 28, 2021), pp. 1684–1696. ISSN: 0006-8950, 1460-2156. DOI: 10.1093/brain/awab088. URL: https://academic.oup.com/brain/article/144/6/1684/6164965 (visited on 08/04/2022).

[58] *Two-Sample t-Test*. URL: https://www.jmp.com/en_ch/statistics-knowledge-portal/t-test/two-sample-t-test.html (visited on 08/04/2022).

[59] Catalyst University. *Mann-Whitney U Test: Theory and Tutorial in Excel*. 2018. URL: https://www.youtube.com/watch?v=7om4YSuq5pw (visited on 08/04/2022).

[60] Hadar Kolb et al. "7T MRI Differentiates Remyelinated from Demyelinated Multiple Sclerosis Lesions". In: *Annals of Neurology* 90.4 (Oct. 2021), pp. 612–626. ISSN: 0364-5134, 1531-8249. DOI: 10.1002/ana.26194. URL: https://onlinelibrary.wiley.com/doi/10.1002/ana.26194 (visited on 08/03/2022).

[61] Oh-Hun Kwon et al. "A framework to analyze cerebral mean diffusivity using surface guided diffusion mapping in diffusion tensor imaging". In: *Frontiers in Neuroscience* 9 (2015). ISSN: 1662-453X. URL: https://www.frontiersin.org/articles/10.3389/fnins.2015.00236 (visited on 08/18/2022).

[62] Nicolas Delinte. "Quantifying the microstructural changes in the brain of patients with alcohol use disorder after abstinence via diffusion MRI". PhD thesis. 2020.

[63] Martina Absinta et al. "Persistent 7-tesla phase rim predicts poor outcome in new multiple sclerosis patient lesions". In: *The Journal of Clinical Investigation* 126.7 (July 1, 2016). Publisher: American Society for Clinical Investigation, pp. 2597–2609. ISSN: 0021-9738. DOI: 10.1172/JCI86198. URL: https://www.jci.org/articles/view/86198 (visited on 08/18/2022).

[64] Reza Rahmanzadeh et al. "A New Advanced MRI Biomarker for Remyelinated Lesions in Multiple Sclerosis". In: *Annals of Neurology* 92.3 (2022). _eprint: https://onlinelibrary.wiley.com pp. 486–502. ISSN: 1531-8249. DOI: 10.1002/ana.26441. URL: https://onlinelibrary.wiley.com/doi/abs/10.1002/ana.26441 (visited on 08/18/2022).

[65] Do Tromp. "DTI Scalars (FA, MD, AD, RD) - How do they relate to brain structure?" In: *The Winnower* (Feb. 29, 2016). DOI: 10.15200/winn.146119.94778. URL: https://thewinnower.com/papers/3524-dti-scalars-fa-md-ad-rd-how-do-they-relate-to-brain-structure (visited on 08/06/2022).

[66] J. S. Lin et al. "Performance Assessment for Brain MR Imaging Registration Methods". In: *American Journal of Neuroradiology* 38.5 (May 1, 2017). Publisher: American Journal of Neuroradiology Section: ADULT BRAIN, pp. 973–980. ISSN: 0195-6108, 1936-959X. DOI: 10.3174/ajnr.A5122. URL: http://www.ajnr.org/content/38/5/973 (visited on 08/07/2022).

[67] Ben Jeurissen et al. "Multi-tissue constrained spherical deconvolution for improved analysis of multi-shell diffusion MRI data". In: *NeuroImage* 103 (Dec. 1, 2014), pp. 411–426. ISSN: 1053-8119. DOI: 10.1016/j.neuroimage.2014.07.061. URL: https://www.sciencedirect.com/science/article/pii/S1053811914006442 (visited on 08/06/2022).

[68] *Multi-shell multi-tissue constrained spherical deconvolution — MRtrix 3.0 documentation*. URL: https://mrtrix.readthedocs.io/en/latest/constrained_spherical_deconvolution/multi_shell_multi_tissue_csd.html (visited on 08/07/2022).

Appendix A

All acquired MRI images

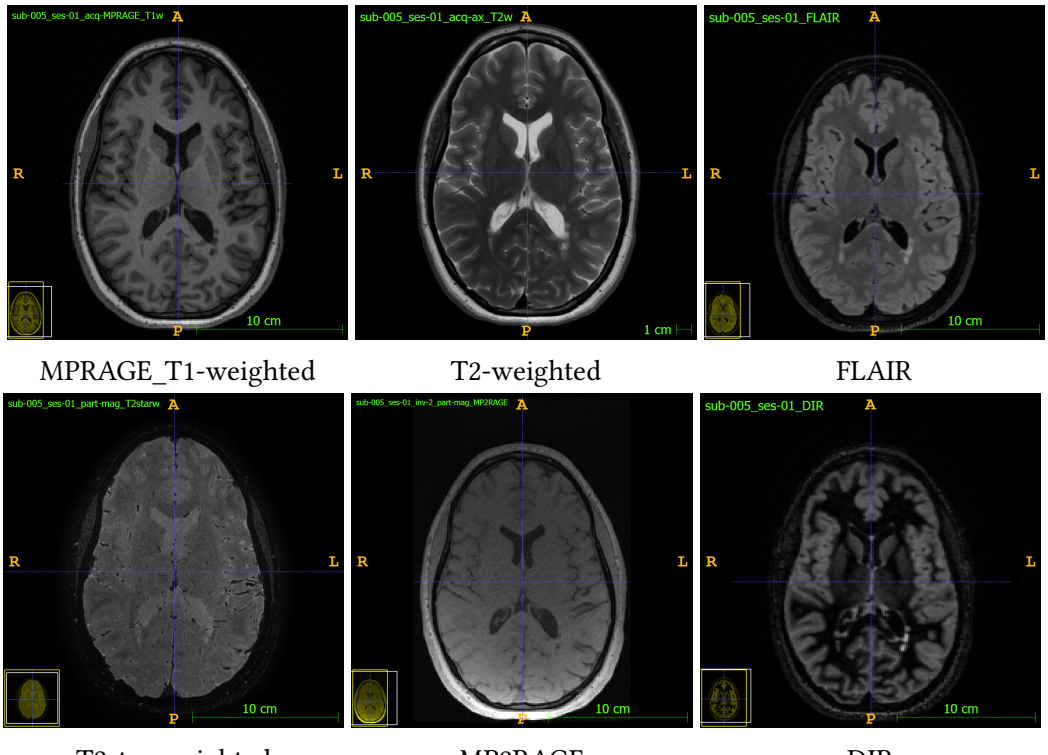

MPRAGE_T1-weighted T2-weighted FLAIR

T2star-weighted MP2RAGE DIR

Figure A.1: All acquired MRI images

UNIVERSITÉ CATHOLIQUE DE LOUVAIN
École polytechnique de Louvain
Rue Archimède, 1 bte L6.11.01, 1348 Louvain-la-Neuve, Belgique | **www.uclouvain.be/epl**